Reaction rate sensitivity of ^{44}Ti production in massive stars and implications of a thick target yield measurement of ^{40}Ca(α,γ)^{44}Ti

R. D. Hoffman[1], S. A. Sheets[1], J. T. Burke[1], N. D. Scielzo[1], T. Rauscher[4], E. B. Norman[1,2,3], S. Tumey[1], T. A. Brown[1], P. G. Grant[1], A. M. Hurst[1], L. Phair[2], M. A. Stoyer[1], T. Wooddy[1], J. L. Fisker[1], D. Bleuel[1]

ABSTRACT

We evaluate two dominant nuclear reaction rates and their uncertainties that affect ^{44}Ti production in explosive nucleosynthesis. Experimentally we develop thick-target yields for the ^{40}Ca(α,γ)^{44}Ti reaction at $E_\alpha = 4.13, 4.54$, and 5.36 MeV using γ-ray spectroscopy. At the highest beam energy, we also performed an activation measurement which agrees with the thick target result. From the measured yields a stellar reaction rate was developed that is smaller than current statistical-model calculations and recent experimental results, which would suggest lower ^{44}Ti production in scenarios for the $\alpha-$rich freeze out. Special attention has been paid to assessing realistic uncertainties of stellar reaction rates produced from a combination of experimental and theoretical cross sections. With such methods, we also develop a re-evaluation of the ^{44}Ti(α,p)^{47}V reaction rate. Using these two rates we carry out a sensitivity survey of ^{44}Ti synthesis in eight expansions representing peak temperature and density conditions drawn from a suite of recent supernova explosion models. Our results suggest that the current uncertainty in these two reaction rates could lead to as large an uncertainty in ^{44}Ti synthesis as that produced by different treatments of stellar physics.

Subject headings: nuclear reactions, nucleosynthesis, abundances $-$ supernovae: general

1. INTRODUCTION

The dynamic synergy between observation, theory, and experiment developed over many years around the field of γ-ray astronomy has as its ultimate goal observations of specifc radionuclides informing our understanding of stellar explosions and the theoretical models that predict nucleosynthesis. Of the radioactive species observed so far, the most long lived, ^{26}Al and ^{60}Fe (with half-lives $\tau_{1/2} = 7.17\pm0.24\times10^5$ and $2.62\pm0.04\times10^6$ yr, respectively), are in reasonably good agreement with theoretical predictions (Timmes et al. 1996; Diehl et al. 2006). Observations of those in the iron group, ^{56,57}Ni ($\tau_{1/2} = 6.075\pm0.01$ d and 35.6 ± 0.06

[1]Lawrence Livermore National Laboratory, 7000 East Avenue, Livermore, CA 94551, USA

[2]Nuclear Science Division, Lawrence Berkeley National Laboratory, Berkeley, CA 94720, USA

[3]Nuclear Engineering Department, University of California, Berkeley, CA 94720, USA

[4]Department of Physics, Basel University, Basel, Switzerland

hr, respectively) and their decay products ^{56,57}Co ($\tau_{1/2} = 77.233 \pm 0.027$ d and 271.74 ± 0.06d, respectively), are used in many ways to constrain our current models of the core collapse explosion mechanism. The radionuclide ^{44}Ti ($\tau_{1/2} = 58.9 \pm 0.3$ yr), made in the same explosive environment but in much lower amounts compared to the very abundant nickle isotopes (Woosley et al. 1973, 1995), is hoped to one day serve as an even more sensitive diagnostic and a valuable probe of the conditions extant in some of the deepest layers to be ejected.

Observationally most of the attention has focused on the detection of the 68, 78, and 1157 keV γ-rays from the ^{44}Ti $\to$ ^{44}Sc $\to$ ^{44}Ca decay chain (see Figure 1). The 1157 keV γ-ray has been observed directly from a point source in Cassiopeia A (Cas A; Iyudin et al. 1994). This was later confirmed by observation of the low-energy ^{44}Sc γ-rays using the *BeppoSax* (Vink et al. 2001) and *INTEGRAL* (Renaud et al. 2006) observatories. Using values for the distance, age, and γ-flux of Cas A, the amount of ^{44}Ti ejected was found to be $1.6^{+0.6}_{-0.3} \times 10^{-4}$ M$_\odot$ (Renaud et al. 2006), in agreement with earlier observations using CGRO (Timmes et al. 1996). Although the presence of ^{44}Ti is currently below detection limits in SN1987A in the nearby Large Magellanic Cloud, its light curve is theorized to now be powered by the decay of ^{44}Ti. The yield of ^{44}Ti in SN1987A has been estimated from its light curve to be $1 - 2 \times 10^{-4} M_\odot$, a factor of 3 greater than predicted by models (Diehl et al. 2006). A third ^{44}Ti source (of lower significance compared to the one in CasA) has been observed in the Vela region (Iyudin et al. 1998) but the existence of a co-located young supernova (SN) remnant has not been confirmed. While the mass of ^{44}Ti observed in SN remnants appears to be underproduced by past models, the number of observed sources of ^{44}Ti in all-sky surveys appears to be less than expected from estimates of the Galactic SN rate and the known ^{44}Ti half life, leading some to question whether ^{44}Ti-producing SNe are exceptional (The et al. 2006).

Theoretically, ^{44}Ti production is traditionally ascribed to regions experiencing a strong "$\alpha-$rich freeze out", where material initially in nuclear statistical equilibrium (NSE) at relatively low density is cooled so rapidly that free $\alpha-$particles do not have time to reassemble, through inefficient $3-$body reactions that span the mass gaps at A=5 and A=8, back into the iron group. A likely scenario is material in or near the silicon shell as it experiences shock wave passage during a core collapse SN event. Assuming the material cools adiabatically over a hydrodynamic timescale ($\tau_{\rm HD} = 446\chi/\sqrt{\rho_i}$), where χ is a scaling parameter (here unity) and ρ_i is the initial (peak) density in g cm^{-3}, initial conditions that would result in a final α-particle mass fraction of $\sim 1\%$ would require temperatures high enough to ensure NSE ($T_{9i} \gtrsim 5$) and an initial density $\rho_i < \min(4.5 \times 10^5 T_{9i}^3, \quad 2.5 \times 10^5 T_{9i}^4 \chi^{-2/3})$ (Woosley et al. 1973). This translates to a radiation entropy greater than unity (Section 3.2).

In models of massive stars the $\alpha-$rich freeze out dominates the solar production of several species, including ^{44}Ca (made as Ti), ^{45}Sc, ^{57}Fe (made as Ni), and ^{58,60}Ni, while still others seem to require a sizable component to account for their solar abundances, including ^{50,52}Cr, ^{59}Co, ^{62}Ni, and ^{64}Zn (Woosley et al. 1995; Thielemann, Nomoto, & Hashimoto 1996). Although ^{56}Ni is the dominant species produced in both NSE and the $\alpha-$rich freez out over a wide range ($0 \leq \eta \leq 0.01$) of neutron excess (Hartmann, Woosley, & El Eid 1985), the solar abundance of ^{56}Fe is dominated by production in explosive silicon burning in massive stars and by a large contribution from SNe Ia (Timmes, Woosley, & Weaver 1995).

In order to address one aspect of the model uncertainties associated with the theoretical predictions of ^{44}Ti in SNe, we focus on exploring the nuclear data uncertainties of two key reaction rates. Experimentally we address the ^{40}Ca(α,γ)^{44}Ti cross section where the existing experimental results are inconsistent and theoretical estimates are complicated by the suppression of $E1$ $T = 0 \to T = 0$ gamma transitions in self-conjugate ($N = Z$) nuclei (Rauscher et al. 2000). This cross section has been measured in the past using several techniques. Cooperman et al. (1977) used in-beam γ-ray spectroscopy to measure the capture of

α-particles on a metallic calcium target in the center-of-mass energy range $E_{CM} = 2.5 - 3.65$ MeV. In that work the excitation function for the 1083 keV first excited state transition in ^{44}Ti was determined and the resonance strengths were developed. Nassar et al. (2006) determined the integral cross section in the range $E_{CM} = 2.2 - 4.17$ MeV by bombarding a He gas target with a ^{40}Ca beam and collecting the recoiling ^{44}Ti in a catcher foil. Accelerator mass spectroscopy was then used to determine the ratio of ^{44}Ti/Ti from the known content of Ti in the catcher foil. Recently, a slightly broader energy range of $E_{CM} = 2.11 - 4.19$ MeV was explored using the DRAGON recoil mass spectrometer (Vockenhuber et al. 2007) in inverse kinematics. They developed individual resonances whose sum was used to determine a reaction rate for $1 \le T_9 \le 5.5$. Yet despite these often heroic expenditures of time, toil, and treasure, in the temperature range of astrophysical interest there still exists a factor of 3 or more difference between the experimentally determined reaction rates.

In this work, we develop the cross section for ^{40}Ca(α,γ)^{44}Ti by two separate methods as a check on systematic uncertainties. First we used in-beam γ-ray spectroscopy to measure a thick target yield of the ^{40}Ca(α,γ)^{44}Ti reaction. We then determined the number of ^{44}Ti nuclei produced by counting low-energy γ-rays from the decay of ^{44}Ti in an irradiated target. Special attention was devoted to checking the internal consistency of the measurements and to establishing realistic uncertainties in developing the stellar reaction rate from a combination of experimental and theoretical cross sections. We have made a similar evaluation of the stellar reaction rate for the dominant destruction reaction, ^{44}Ti(α,p)^{47}V, based on the original experimental work of Sonzogni et al. (2000) and the theoretical cross section work of Rauscher & Thielemann (2001).

Our results are presented in four parts. In Section 2, we describe our experimental efforts. Section 3 then discusses the development of stellar reaction rates, and an expose of the past and present experimental and theory efforts for the two rates in question. In Section 4, we present nucleosynthesis results for the production of ^{44}Ti and ^{56,57,58}Ni reported in previous surveys of massive star evolution. We then carry out a sensitivity survey of ^{44}Ti to variations in the principle production and destruction rates using more recent SN models. In Section 5 we provide a discussion and conclusions.

2. Experimental Methods

The ^{40}Ca(α,γ)^{44}Ti reaction was measured at the Lawrence Livermore National Laboratory (LLNL) Center for Accelerator Mass Spectroscopy (CAMS) using a 10 MV FN Tandem Van de Graaff accelerator. To calibrate the beam energy a silicon detector was placed in a low current beam and the measured energy was then compared with spectroscopy grade α-sources. The α energies used were the 5.30 MeV from ^{210}Po, the 6.12 MeV from ^{252}Cf, the 5.49 MeV from ^{241}Am, and the 4.69 and 4.61 MeV α's from the decay of ^{230}Th. From the calibration, the uncertainty in the α-beam energy is $\pm$ 5 keV. The thick target yield was measured at $E_\alpha = 4.13$, 4.54, and 5.36 MeV beam energies.

For each beam energy a target was manufactured by pressing ^{nat}CaO powder[1] into a copper holder. The powder had a purity of 99.95% (metals basis) but contained ppm concentrations of C and F. To completely stop the beam, each target had a minimum thickness of at least 1.1 mm. The target was mounted on a copper block within the vacuum chamber and tilted at 30° with respect to the beam. The vacuum chamber contained two windows so that the target could be visually monitored. A schematic of the target chamber

---

[1]Obtained from Alfa Aesar, MA, USA

is given in Figure 2.

The target chamber was electrically isolated from the rest of the beam line. The target was electrically connected to the target chamber allowing the beam current to be directly measured from the chamber. The current integration from the target chamber was checked to a precision of better than 1% using a NIST-traceable precision DC current source. An opposing-pair magnet was attached upstream of the target chamber to suppress the escape of secondary electrons generated by the beam on the target. A summary of the irradiation runs is given in Table 1.

Two 80% HPGe detectors were used to measure the prompt γ-ray yield during irradiation. One detector was 11.4 cm away from the target at 30° with respect to the beam. The location of the second detector was at 15.8 cm and an angle of 99°. The HPGe detector thresholds were set at 125 keV. The average deadtime during a run was 10 %.

The γ-ray energy spectra was accumulated in 8192 channels using two Ortec AD413a ADCs. Efficiency and energy calibrations of the HPGe detectors were made using ^{60}Co, ^{22}Na, ^{137}Cs, ^{54}Mn, and ^{133}Ba NIST-traceable sources with activities known to a 1σ uncertainty of 1%. Efficiencies of 0.085% and 0.162% were found for the detectors at 30° and 99°, respectively.

2.1. Analysis of Prompt γ-Ray Data

The thick target yield for the ^{40}Ca$(\alpha,\gamma)^{44}$Ti reaction was deduced from the yield of the $2^+\rightarrow0^+$ 1083 keV transition which collects most of the strength from ^{44}Ti. The angular distribution of the 1083 keV γ-rays with respect to the angle between the γ-rays and beam direction is given by $W(\theta) = \sum_l a_l P_l(\cos\theta)$ with $l = 0$, 2, 4. The cross section is proportional to a_0 so only this term needs to be determined (Dyer et al. 1981). By placing the detectors at angles for which $P_4(\cos\theta)$ is zero, 30.6° and 109.9°, a_0 can be determined from measurements at only two angles. The experimental thick target yield of the 1083 keV γ-ray at angle θ is given by

$$Y_{1083}(\theta) = \frac{N_c}{N_p L_t A_b \, \varepsilon_{1083}}, \tag{1}$$

where N_c is the number of counts in the 1083 keV photopeak, N_p is the number of α particles impinging on the target, L_t is the detector live-time fraction, A_b is the natural abundance of ^{40}Ca, and ε_{1083} is the efficiency of the HPGe detector at 1083 keV. The region near the 1083 keV γ-ray is shown in Figure 3 for E_α = 5.36 MeV. The 1083 keV photopeak lies on the tail of the 1039 keV ^{70}Ge doppler shifted γ-ray excited by fast neutrons primarily from the ^{19}F(α,n) reaction. The background and 1083 keV peak were fit to an error function convoluted with a Gaussian, as in Gete et al. (1997). The total experimental yield for the 1083 keV γ-ray was determined by finding a_0 from the angular distribution of $Y(\theta)$. The experimental yield of the 1083 keV γ-ray determined from these fits are given in Table 2. In order to convert the yield of the 1083 keV γ-ray into the yield of ^{44}Ti, one must take into account those transitions which bypass the $2^+ \rightarrow 0^+$ 1083

Table 1.   Irradiation Conditions for the $^{\rm nat}$CaO Targets.

Irradiation Run	E_α (MeV)	Irradiation Time (hr)	Total Charge (μC)
1	4.13	6	45808.6
2	4.54	7	46115.8
3	5.36	10	25763.2

keV transition in ^{44}Ti. The Monte Carlo program DICEBOX (Becvar 1998) was used to simulate the γ-ray cascades from the decay of the compound nucleus ^{44}Ti in order to estimate the number of transitions which bypass the $2^+ \rightarrow 0^+$ transition. These simulations suggest $(20 \pm 3)\%$ of transitions bypass the $2^+ \rightarrow 0^+$ transition with the error on the simulations taking into account the uncertainty in the nuclear level density, the photon strength function, and the capture state. In Figure 4, the thick target yield corrected for the missed strength to the 1083 keV level is compared to the NON-SMOKER cross section.

The experimental yield can be related to a theoretical cross section $\sigma(E)$ by the equation

$$Y = \int_0^{E_\alpha} \frac{\sigma(E)}{-dE/dx} dE \tag{2}$$

where $\sigma(E)$ is the energy-dependent cross section, and dE/dx is the stopping power for $^{\rm nat}$CaO. The dE/dx values for $^{\rm nat}$CaO were calculated using the program SRIM (J.F. Ziegler 2004). Table 2 gives a comparison of the experimental and calculated yields using the NON-SMOKER Hauser-Feshbach ^{40}Ca$(\alpha,\gamma)^{44}$Ti cross section (Rauscher & Thielemann 2001). The experimental yields are a factor of 1.7-2.3 times smaller than the yield calculated from the theoretical cross sections.

The uncertainties from detector efficiencies, deadtime, angular distribution corrections, coincidence summing, and beam current integration are tabulated in Table 3. The integrated beam current was cross checked by using the ^{17}O$(\alpha,\alpha'\gamma)$ and ^{44}Ca$(\alpha,\alpha'\gamma)$ reactions. The thick target yield for the ^{17}O$(\alpha,\alpha'\gamma)$ reaction that excites the first excited state at 870.8 keV was measured in Hsu (1982) at $E_\alpha = 5.486$ MeV. Using Equation (1), N_p from ^{17}O$(\alpha,\alpha'\gamma)$ was determined to be $(7.2\pm0.86)\times10^{16}$ after correcting for the difference in beam energy between Hsu (1982) and our work. The thick target yield for the Coulomb excitation of the 1157 keV level in ^{44}Ca was calculated using the program GOSIA (Czosnyka et al. 1983) and used to infer N_p of $(8.2\pm1.6)\times10^{16}$. This compares well with our beam current integrator which gave a value of 7.2×10^{16} for N_p. The efficiency of the detector at $30°$ was sensitive to the decay location due to the attenuation of γ-rays through the copper target holder. By varying the position of γ-ray sources to match the approximate 1 cm^2 beam spot size the uncertainty in the efficiency was determined. The uncertainty due to coincidence summing of γ-rays in a single detector was estimated from the geometric solid angle spanned by the detectors.

The angular distribution is the largest source of uncertainty. Our detectors did not sit at exactly the zeros of the P_4 term in the angular distribution which introduces some uncertainty when a_0 is determined with only two detectors. Furthermore, Simpson et al. (1971) measured the angular distribution of γ-rays following resonance α capture at $E_\alpha = 4.22$, 4.26, and 4.52 MeV and found a strong contribution for the P_4 term. The uncertainty on a_0 was estimated by the following procedure. A value was chosen for the a_4 coefficient between ±0.5 and then a fit of the angular γ-ray yield was made. The resulting variation in a_0

Table 2. ^{40}Ca$(\alpha,\gamma)^{44}$Ti Measured and Theoretical Thick Target Yields per α Particle on Target. Y_{1083} is the measured yield for the 1083 keV γ-ray, $Y_{^{44}{\rm Ti}}$ is the total yield for the production of ^{44}Ti, and $Y_{\rm theory}$ the thick target yield calculated from Equation 2 assuming the theory cross section of Rauscher & Thielemann (2001). $Y_{\rm offline}$ is the yield from our activation measurement of the target irradiated at 5.36 MeV.

E_α (MeV)	Y_{1083} (10^{-11})	$Y_{^{44}{\rm Ti}}$ (10^{-11})	$Y_{\rm theory}$ (10^{-11})	$Y_{\rm offline}$ (10^{-11})
4.13	2.11 ± 0.40	2.53 ± 0.50	5.96	
4.54	5.72 ± 1.1	6.86 ± 1.4	16.4	
5.36	29.2 ± 5.7	35.0 ± 7.1	61.0	35.7 ± 2.5

was between 17% and 18% for different values of a_4. This is a conservative estimate because the many γ-ray cascade paths and alpha energies involved are likely to wash out any nuclear alignment and would cause a_4 to be nearly zero.

2.2. Low Background Counting

The offline counting of the irradiated target took place at the Low Background Counting facility at LLNL. Only the target irradiated at $E_\alpha = 5.36$ MeV was counted because the activity of the other targets was estimated to be too low. A HPGe low-energy photon spectrometer (LEPS) detector was used to detect 68 and 78 keV γ-rays from ^{44}Ti decay. The target was placed 2 mm away from the detector face and counted for two weeks. The activity of the ^{44}Ti target was determined by comparing it to a 56.6 ± 1.6 nCi ^{44}Ti reference source. The reference source was counted with the LEPS detector in the same geometry as the ^{44}Ti target.

The ^{44}Ti reference source strength was determined by using an 80% HPGe detector to compare the 1157 keV γ-ray to a ^{22}Na and ^{60}Co calibrated source. The count was made at a distance of 60 cm away from the detector in order to avoid summing of the 1157 keV γ-ray with the 511 keV γ-ray.

The yield was found from

$$Y = \frac{A\,T_{\frac{1}{2}}}{N_p \ln 2},\tag{3}$$

where A is the activity of the irradiated target and $\tau_{1/2} = 58.9 \pm 0.3$ years is the ^{44}Ti half-life (Ahmad et al. 2006).

A simultaneous fit of the peaks in Figure 5 gives an experimental yield of $(35.7 \pm 2.5) \times 10^{-11}$ ^{44}Ti per α-particle. The uncertainty in the offline yield takes into account the uncertainty in the detector efficiency, half-life, integration of beam current, calibration source strength, and statistics. Since the activity of the ^{44}Ti target was determined with a reference source having the same decay scheme the need to correct for summing of the 68 and 78 keV γ-rays was eliminated. This yield is 22% higher than the yield from the online counting and agrees with the estimate that $(20\pm3)\%$ of γ-ray cascades bypass the 1083 keV level. This also demonstrates that sputtering of the target was minimal during particle bombardment.

Table 3.   Compilation of systematic uncertainties for the online measurement (1σ).

Source of uncertainty	Uncertainty
Beam integration	1%
Detector efficiency	6%-7%
Deadtime	1%
Angular distribution	17%-18%
Coincidence summing	1%

3. Reaction Rates

3.1. The True Gamow Window

Thermonuclear reaction rates are obtained through integration of the energy-dependent cross section weighted by a Maxwell-Boltzmann (MB) particle distribution (Fowler, Caughlan & Zimmerman 1967). For reaction $I^\mu(j,k)L^\nu$

$$N_A\langle\bar{\sigma}^\mu_{jk}v\rangle = \frac{3.732\times10^{10}}{\hat{A}_j^{1/2}T_9^{3/2}}\int_0^\infty \bar{\sigma}^\mu_{jk}E_j^\mu\exp(-11.605E_j^\mu/T_9)dE_j^\mu \tag{4}$$

where N_A is Avagadro's number, $\hat{A}_j \sim 3.64$ is the reduced mass of the target and incident projectile in atomic mass units, μ is an index representing bound states in the target and product nuclei ($\mu = 0$ for the ground state, 1 for first excited, etc.), and v is the relative velocity of the α-particle (j) and the target (I^μ) in cm s^{-1}. The cross section $\bar{\sigma}^\mu_{jk}$ is expressed in barns, E_j^μ is the center of mass energy of the α-particle and the target in MeV, T_9 is the temperature in billions of degrees Kelvin, and the reaction rate has units of cm^3 mole^{-1} s^{-1}.

There are two important issues regarding the cross section $\bar{\sigma}^\mu_{jk}$ used in the integration and its relation to the experimental cross section. First, when computing *astrophysically relevant* reaction rates, the cross section has to be the one for a thermally excited target nucleus in the plasma. Only such a stellar cross section allows application of detailed balance to derive the reverse rate (Holmes et al. 1976; Rauscher et al. 2009). Laboratory cross sections are measured with the target nucleus in the ground state only and the correction, or stellar enhancement factor, has to be calculated from theory. For the ^{40}Ca$(\alpha,\gamma)^{44}$Ti and ^{44}Ti$(\alpha,p)^{47}$V reactions the correction factors are unity over the entire temperature range of interest (Rauscher & Thielemann 2000). Therefore the cross section $\bar{\sigma}^\mu_{jk}$ is identical to the cross section σ appearing in Eq. 2.

Second, the question arises as to how well the reaction rate is constrained by the experimental cross section data. In the rare case of a thick target yield measurement that completely samples the relevant stellar temperature range, a direct calculation of the thermonuclear reaction rate can be obtained by introducing a simple change of variable and combining Eq.'s 2 and 4 (Roughton et al. 1976). More often limitations of the experimental apparatus and/or beam time allotment restricts the measurement of cross section data to a fairly narrow energy range. To produce a reaction rate spanning a realistic temperature range for stellar synthesis, one often has to supplement the experimental results with theory cross section values to perform the integration in Eq. 4. The integrand exhibits a maximum contributing most to the reaction rate due to the folding of the energy-dependences of the cross section and the MB distribution. Conventionally, the location and width of this Gamow peak are estimated by multiplying a Coulomb barrier penetration factor with the high-energy tail of the MB distribution or by considering a Gaussian approximation to it (see, e.g., Clayton (1984); Rauscher (2010)).

However, this is applicable for capture reactions only as long as the γ-width is larger than the charged particle width (Iliadis 2007). Since the α width is changing rapidly with energy due to the Coulomb barrier, this prerequisite may only be fulfilled at very low projectile energies which effectively shifts the Gamow window to lower energies than expected from the standard approximation formula. Figure 6 confirms this by showing the "true" Gamow window at $T_9 = 2$ and $T_9 = 5$ in comparison to the peaks obtained from the standard formula and its approximation for the ^{40}Ca$(\alpha,\gamma)^{44}$Ti and ^{44}Ti$(\alpha,p)^{47}$V reactions. Finally, Fig. 7 compares the energy range spanned by our experimental data with the true Gamow window for stellar temperatures $1 \leq T_9 \leq 5$. The width of the window is defined such that filling the "window" with experimental data would determine the reaction rate to 10% accuracy. The minimum temperature at which

an experiment can fully inform the reaction rate is the overlap of the full width of the window and the range of experimental data (shaded region). For the astrophysical processes considered here, the most relevant temperature range is between $2.0 \leq T_9 \leq 4.0$ (Section 3.4). A less severe situation exists for the $^{44}\text{Ti}(\alpha, p)^{47}\text{V}$ (Figure 8). From these figures it is evident that the limited range of experimental data collected in these two experiments do not contribute significantly to the rates in the important temperature range and that the supplemental theory cross sections at lower energies will dominate both of the rates and their uncertainties. Nevertheless, the data can be used to test the NON-SMOKER predictions at higher energies.

3.2. Reaction Rate for $^{40}\text{Ca}(\alpha, \gamma)^{44}\text{Ti}$

To obtain a "semi-experimental" astrophysical rate for $^{40}\text{Ca}(\alpha, \gamma)^{44}\text{Ti}$, we normalized the NON-SMOKER cross section by a factor of 1.71 to agree with our measured thick target yield at 5.36 MeV (Figure 4). The data at this energy were chosen because the experimental result was confirmed by two independent techniques. Although the errors on the experimental thick target yield are small, during the calcuation of the reaction rate we have to assign an uncertainty which is similar to the uncertainty on the theory cross section. Therefore we will perform our astrophysical studies with an assigned factor of 2 uncertainty on this rate. This also accounts for a potentially different energy-dependence of the theoretical cross section, and fits well with the general factor of $2 - 3$ accuracy expected for global predictions of low-energy α-capture reactions on self-conjugate nuclei (Rauscher et al. 2000).

The resulting reaction rates were then fit assuming the REACLIB parameterization (Rauscher & Thielemann 2001).

$$N_A < \sigma\nu >= \exp(a_0 + a_1 T_9^{-1} + a_2 T_9^{-1/3} + a_3 T_9^{1/3} + a_4 T_9 + a_5 T_9^{5/3} + a_6 \ln(T_9)) \tag{5}$$

where T_9 is the temperature in 10^9 K. The fit is defined in the range $0.01 \leq T_9 \leq 10.0$. The reverse rate for $^{44}\text{Ti}(\gamma, \alpha)^{40}\text{Ca}$ is calculated through detailed balance, the Q value of the forward reaction is 5.1271 MeV.

Figure 9 shows the $^{40}\text{Ca}(\alpha, \gamma)^{44}\text{Ti}$ reaction rates considered in this study. The values are generated from fits to reaction rates developed from numerous experimental and theory efforts carried out over the last 20 years. Some have been used in widely cited nucleosynthesis surveys. In particular, Woosley et al. (1995) utilized the theory rates from Woosley et al. (1978), while Limongi & Chieffi (2006) used the fit published in Rauscher & Thielemann (2000). Rauscher et al. (2002) used this same fit but normalized at $T_9 = 3$ to the "empirical" rate developed in Rauscher et al. (2000). Only "experimentally" determined rates are shown in the main panel, along with the tabulated Hauser-Feshbach theory based rate (crosses) of Rauscher & Thielemann (2001), hereafter referred to as NON-SMOKER. Also plotted in the inset is the ratio of each rate versus the NON-SMOKER rate, our recommended $^{40}\text{Ca}(\alpha, \gamma)^{44}\text{Ti}$ rate lies between the oldest and most recent experimental results.

For ^{44}Ti synthesis the most relevant temperature range is $2.0 \leq T_9 \leq 4.0$. Over this range *experimental* $^{40}\text{Ca}(\alpha,\gamma)^{44}\text{Ti}$ rates vary by factors of 3-5, respectively. The two most recent experimental rates (Nassar et al. 2006; Vockenhuber et al. 2007) are larger than our recommended rate and would suggest *increased* ^{44}Ti synthesis over our result and the yet smaller original experimental result of Cooperman et al. (1977).

The range of variation in the theory rates is also large, that of Woosley et al. (1978) being of the order of the largest experimental results, the smallest is clearly that of Rauscher & Thielemann (2000). Most unfortunately, the rate generated from this published fit differs from the tabulated NON-SMOKER rate (crosses) by factors of 2 (high and low) on both ends of the important temperature range. Rauscher & Thielemann (2000) fit this rate to an accuracy of 0.92 over the temperature range $0.1 \leq T_9 \leq 10$. In general fits to

charged particle rates have larger deviations than those for neutron-induced reactions. Most often a quote of low accuracy pertains to deviation at the lowest temperature points of the fit. Based on arguments related to the nuclear level density and its impact on the applicability of the statistical model, Rauscher & Thielemann (2000) suggest that the lower limit of applicability for this dominant production rate is $T_9 = 0.24$, well below the important temperature range in this study. To be fair the statistical result itself could well be in error by a factor of 2 or more due to the uncertainty in the global α+nucleus optical potential, and the fit does agree at $T_9 = 2.8$, which is close to the midway point of ^{44}Ti production in several of the scenarios studied in the next section. We have re-fit this rate (dotted line in the inset), and observe that over the important temperature range it now differs from the NON-SMOKER rate by no more that 12% (typically better than 5%). We will include both fits in our sensitivity analysis.

With an uncertainty of a factor of 2, our new "semi-experimental" rate encompasses most of the previous experiments and calculations. This underlines the necessity for further measurements in the relevant astrophysical energy range (2-5 MeV).

3.3.   Reaction Rate for ^{44}Ti$(\alpha, p)^{47}$V

Figure 10 shows a similar comparison for the ^{44}Ti$(\alpha, p)^{47}$V rates. As with the dominant production rate, the original Rauscher & Thielemann (2000) fit to this destruction rate is in poor agreement with the statistical NON-SMOKER rate (crosses). They list a fit uncertainty of 0.12 and the lower limit of applicability as $T_9 = 0.035$, again outside the important temperature range in this study. We also note that the NON-SMOKER rate exceeds the older (dot-long-dash line) statistical result of Woosley et al. (1978) for $T_9 \geq 2.4$, which would suggest *decreased* ^{44}Ti production over that seen in the survey of Woosley et al. (1995).

The only published experimental reaction rate (Sonzogni et al. 2000) is roughly a factor of 2 above the NON-SMOKER rate, which would suggest even *further decreased* ^{44}Ti synthesis compared to the previously available theory rates. To generate their reaction rate Sonzogni et al. (2000) interpolated their four cross section points between $E_{\rm c.m.} = 5.7$ and 9.0 MeV, extended the energy range above and below these values with scaled cross sections from SMOKER (Thielemann, Arnould, & Truran 1987), and then integrated over a MB distribution to obtain the reaction rate and produced a REACLIB fit to it. They claim agreement with the calculated rate of 43% at the highest temperatures and 30% at $T_9 = 2.5$. Interestingly, their derived experimental rate shows a very different temperature dependence compared to the reaction rates of Rauscher & Thielemann (2001) and Woosley et al. (1978), suggesting a very different energy dependence of the cross section. This result is very surprising as the energy dependence of the SMOKER cross section is very similar to that of the NON-SMOKER cross section. Sonzogni et al. (2000) provide plots of their experimental values and calculated cross section between 5 and 10 MeV, and the fit of their reaction rate versus SMOKER and Woosley et al. (1978), but unfortunately no further details. Considering Figures 6 and 8 of Sonzogni et al. (2000), it is clear that their reaction rate for $2.5 \leq T_9 \leq 5$ was determined completely by the scaled SMOKER cross section values.

We provide a re-evaluation of the rate from the data of Sonzogni et al. (2000) which also includes an increased uncertainty estimate. Since the experimental data (within errors) lies within 20% of the NON-SMOKER cross section prediction, we generated a set of hybrid cross sections by supplementing the experimental ones with *unrenormalized* NON-SMOKER values above and below the experimental energy range. We assigned a factor of 2 uncertainty to the theory values above the experimental data and a factor of 3 below. For the experimental data points we assigned the errors on energy and cross section as given in

Sonzogni et al. (2000). The code EXP2RATE (Rauscher 2003-2009) allows one to calculate reaction rates from cross sections (or astrophysical S-factors) that include both theoretical uncertainties and experimental error bars. The ratio of the resulting rate with its uncertainty range to the NON-SMOKER rate is shown in Fig. 11. Again, the experimental data contribute to the rate integral only at higher temperatures and the standard NON-SMOKER rate is still well within the uncertainty even at those temperatures. In our sensitivity study we adopt the geometric mean of the upper and lower rate limit as our "recommended" rate and consider a variation of a factor of 3 (up and down) as a reasonable uncertainty estimate based on inspection of the uncertainty limits in the relevant temperature range.

Note that our semi-experimental rate for ^{44}Ti$(\alpha, p)^{47}$V is fit in the endoergic $(-Q)$ direction while the original theory rates (Rauscher & Thielemann 2001; Woosley et al. 1978) were fit in the exoergic $(+Q)$ direction. Reaction rates for targets in their ground states alone (or any distribution other than thermal equilibrium) *do not obey reciprocity* because the forward and reverse reactions are not symmetrical (Holmes et al. 1976). Thus it is very important to measure cross sections for astrophysical application in the direction that is least affected by excited state effects in the target, which is almost always in the exoergic direction. This particular reaction is an exception in that it has a small reaction Q value $(-0.410$ MeV$)$ and excited state effects that are minimized by Coulomb suppression of the stellar enhancement factor. See Kiss et. al. (2008) and Rauscher et al. (2009) for details.

In Table 4, we provide fits in the REACLIB format for all of the rates discussed above. For nasr06 (Nassar et al. 2006) the reaction rate values we fit were themselves generated from a fit supplied in that paper, otherwise we have used (and always recommend) tabulated values where available, as we have done for rath01 (Rauscher & Thielemann 2001), coop77 (Cooperman et al. 1977), and wfhz78 (Woosley et al. 1978). The rates labeled "hsr10" are our evaluated rates from our own experimental work and our re-evaluation of the rate from Sonzogni et al. (2000). For voch07 (Vockenhuber et al. 2007) we fit their central "Rate" tabulated between $1 \leq T_9 \leq 5.5$ (see their Table III). For each fit we define a measure of accuracy, ζ, between the rate r_i and the fit f_i for the seven T_9 temperature points 1.0, 1.5, 2.0, 2.5, 3.0, 3.5, and 4.0 as

$$\zeta = \frac{1}{n}\sum_{i=1}^{7}\left(\frac{r_i - f_i}{f_i}\right)^2 \tag{6}$$

We also supply the reverse rate fits in the REACLIB format. *These must be multiplied by the appropriate ratio of nuclear partition functions* as specified and tabulated in Rauscher & Thielemann (2000). Again, the re-evaluated and re-fit rates for ^{44}Ti$(\alpha, p)^{47}$V must be inserted into REACLIB in the forward rate direction (increasing mass or charge).

Of course many other nuclear reaction rates affect ^{44}Ti synthesis. A prioritized list was suggested by The et al. (1998), but only for one choice of peak temperature and density $(T_{9p} = 5.5, \quad \rho_p = 1.0 \times 10^7$ g cm$^{-3})$ and three values of electron fraction $(Y_e = 0.5, 0.499,$ and $0.497)$. Recently the NuGRID team has presented a preliminary survey of ^{44}Ti synthesis over a wide range of peak temperature and density conditions for $Y_e = 0.5$ in which they define several regions where a similar set of reaction rates are suggested to be more effective than others (Magkotsios et al. 2008).

For this study we used the reaction rate library developed by Hoffman et al. (2002). We only explore variations in ^{44}Ti synthesis due to the dominant production and destruction rates mentioned above, but here cite our sources for several other key reactions noted by The et al. (1998) and Magkotsios et al. (2008).

For important rates that produce ^{44}Ti we adopted the 3α reaction rate of Caughlan & Fowler (1998). Coupled with their ^{12}C$(\alpha, \gamma)^{16}$O rate uniformly multiplied by a factor of 1.7 (corresponding to an S-factor at

300 keV of 170 keV barns), these proved optimal for producing the solar abundance set (Timmes, Woosley, & Weaver 1995). Although we do not explore variations in these rates, we acknowledge their importance, especially the former, in setting the α-abundance on which both ^{40}Ca and ^{44}Ti production depend. This choice is not critical to showing the sensitivity of ^{44}Ti to the two rates we concentrate on. As previously mentioned we developed a new semi-experimental rate for ^{40}Ca$(\alpha,\gamma)^{44}$Ti with a factor of 2 uncertainty and also consider six alternate reaction rates (Figure 9). We also adopted rates for the weakly competing side chain ^{40}Ca$(\alpha, p)^{43}$Sc and ^{43}Sc$(p, \gamma)^{44}$Ti from Rauscher & Thielemann (2000).

The dominant ^{44}Ti destruction rate in this study was ^{44}Ti$(\alpha, p)^{47}$V. We explore three choices, our re-evaluated Sonzogni et al. (2000) rate with uncertainty factors 3 and 1/3 as upper and lower limits. Other destruction reactions of note were ^{44}Ti$(p, \gamma)^{45}$V and ^{45}V$(p, \gamma)^{46}$Cr, both taken from Fisker et al. (2001). Finally ^{44}Ti$(\alpha, \gamma)^{48}$Cr was taken from Rauscher & Thielemann (2000).

In the following section we adopt our recommended "semi-experimental" rates as the default production and destruction rates when we report specific values in our nucleosynthesis survey.

4. Nucleosynthesis Studies

4.1. Initial Conditions

Previous efforts to explore the sensitivity of ^{44}Ti synthesis to the ^{40}Ca$(\alpha,\gamma)^{44}$Ti reaction rate have often been confined to one-zone parameterized network simulations for a limited number of initial conditions (The et al. 1998; Vockenhuber et al. 2007). A much larger survey promises to explore ^{44}Ti synthesis over a wider range of initial conditions (Magkotsios et al. 2008). From this survey we choose eight points that reflect peak conditions experienced in various SN explosion models that span the regimes from incomplete silicon burning to the α-rich freeze out (see Table 5). Ideally one would prefer to explore rate sensitivity in full star models of stellar evolution (Nassar et al. 2006), but for species that are made under a limited range of stellar conditions that do not involve details affected strongly by the stellar physics, such as burning over long time-scales in convective regions, one zone calculations are usually adequate as long as a reasonable range of conditions are explored. We take this approach.

Our calculations are straight-forward. Table 5 lists our choices for peak temperature and density. From these we calculate the hydrodynamic time-scale, $\tau_{\rm HD} = 446\chi/\sqrt{\rho_p}$ and the radiation entropy, $S_{\rm rad} = 3.33 \times T_{9p}^3/\rho_{5p}$, where $\rho_{5p} = 10^{-5} \times \rho_p$ g cm^{-3} and S is in units of Boltzmann constant per baryon (hereafter we refer to entropy without its units). For the hydrodynamic timescale χ is a scaling parameter (assumed to be unity unless explicitly stated). The material then expands adiabatically ($\rho \propto$ T^3) with $\rho(t) = \rho_p \exp(-t/\tau)$ on a hydrodynamic time-scale until the temperature declines to $T_9 \sim 0.25$, a point where all charged particle reactions affecting ^{44}Ti synthesis have frozen out. The last column (t_χ) gives the approximate time for each simulation to terminate based on the scale factor for the hydrodynamic time-scale. We will explore two values, $\chi = 1$ and 5. The initial compositions consist of neutron, proton, and $\alpha-$particle mass fractions that provide for a specific neutron excess $\eta = \sum_i(N_i - Z_i)(X_i/A_i)$ where N_i, Z_i, A_i and X_i are the neutron, proton, atomic mass number, and mass fraction of the isotope i with $\sum_i X_i = 1$. The neutron excess is related to the electron mole number via $Y_e = 1 - 2\eta$. For each initial condition we will survey a range of neutron excess ($-0.01 \leq \eta \leq 0.03$) as well as variations in two specific reaction rates.

Our peak conditions were chosen to reflect the sensitivity of the nucleosynthesis to variations in entropy and expansion timescale. According to Magkotsios et al. (2008), points CasA $1 - 3$ lie along the track of a

Table 4.   Reaction Rate Fit Parameters for $^{40}\text{Ca}(\alpha,\gamma)^{44}\text{Ti}$ and $^{44}\text{Ti}(\alpha,p)^{47}\text{V}$

a_0	a_1	a_2	a_3	a_4	a_5	a_6	ζ	Author
$^{40}\text{Ca}(\alpha,\gamma)^{44}\text{Ti}$								
87.90966	0.82813	-71.88292	-38.54585	0.23930	0.09330	12.74610	2.71e-04	nasr06
0.72761	-19.77781	-3.31217	1.72317	-1.92089	0.13943	7.44775	1.43e-04	voch07
98.50815	1.14177	-77.63240	-44.20413	0.92480	0.04292	12.16306	2.03e-03	hsr10hi
97.82161	1.14060	-77.59144	-44.25277	0.92716	0.04280	12.18964	2.03e-03	hsr10rec
97.13505	1.13944	-77.55049	-44.30142	0.92953	0.04267	12.21624	2.03e-03	hsr10lo
-102.45950	-34.96400	62.07089	57.31170	-5.70439	0.32517	-0.02072	6.45e-03	coop77
85.44962	0.67896	-73.40626	-34.23476	-0.04774	0.09442	10.65082	6.63e-03	rath01
78.50683	0.41907	-68.31831	-31.11664	-0.88984	0.16873	11.80039	8.15e-03	wfhz78
$^{44}\text{Ti}(\gamma,\alpha)^{40}\text{Ca}$								
112.85950	-58.66788	-71.88292	-38.54585	0.23930	0.09330	14.24610		nasr06
25.67748	-79.27381	-3.31217	1.72317	-1.92089	0.13943	8.94775		vock07
123.45800	-58.35423	-77.63240	-44.20413	0.92480	0.04292	13.66306		hsr10hi
122.77150	-58.35540	-77.59144	-44.25277	0.92716	0.04280	13.68964		hsr10rec
122.08490	-58.35656	-77.55049	-44.30142	0.92953	0.04267	13.71624		hsr10lo
-77.50965	-94.46000	62.07089	57.31170	-5.70439	0.32517	1.47928		coop77
110.39950	-58.81704	-73.40626	-34.23476	-0.04774	0.09442	12.15082		rath01
$^{44}\text{Ti}(\alpha,p)^{47}\text{V}$								
-16.17831	-7.55203	-3.97859	7.78213	-3.73270	0.26210	17.63160	1.43e-05	hsr10hi
-35.62246	-9.04965	5.56533	18.44151	-4.10095	0.24244	16.05165	1.16e-03	hsr10rec
-55.06717	-10.54735	15.10957	29.10119	-4.46916	0.22277	14.47158	4.16e-03	hsr10lo
-5.77460	-7.03160	-9.79294	0.64303	-2.72164	0.19070	17.68239	8.12e-05	rath01
$^{47}\text{V}(p,\alpha)^{44}\text{Ti}$								
-14.90159	-2.81742	-3.97859	7.78213	-3.73270	0.26210	17.63160		hsr10hi
-34.34573	-4.31504	5.56533	18.44151	-4.10095	0.24244	16.05165		hsr10rec
-53.79045	-5.81274	15.10957	29.10119	-4.46916	0.22277	14.47158		hsr10lo
-4.49788	-2.29699	-9.79294	0.64303	-2.72164	0.19070	17.68239		rath01

Table 5.   Nucleosynthesis Survey - Peak Initial Conditions

Point	Model	T_{9p}	ρ_{7p}	S_{rad}	τ_{HD}	$t_{\chi=1}$	$\tau_{\text{HD}} \times 5$	$t_{\chi=5}$
		10^9 K	10^7 g cm^{-3}	k^{-1}	sec.	sec.	sec.	sec.
1	CasA	6.5	0.4	22.8	0.22	2.1	1.10	10.8
2	CasA	5.5	0.2	27.7	0.32	2.9	1.60	14.3
3	CasA	4.7	0.1	34.5	0.45	3.9	2.25	18.0
4	2DExpl	6.5	1.0	9.14	0.14	1.3	0.70	6.5
5	2DExpl	5.5	1.0	5.54	0.14	1.3	0.70	6.5
6	2DExpl	4.7	1.0	3.45	0.14	1.2	0.70	6.5
7	2DMHD	6.5	10.0	0.91	0.04	0.42	0.20	2.1
8	2DMHD	5.5	10.0	0.55	0.04	0.41	0.20	2.1

model for Cassiopia A and have very similar entropy values near 30, they differ from one another by a factor of 1.5 (33%). Points 2DExpl $4-6$ are from a rotating two-dimensional explosion model (point 5 closely corresponds to a point along the track of a Gamma-ray Burst model), while points 2DMHD-7 and -8 lie along the track of a two-dimensional rotating MHD star (point 7 samples the "Chasm" region where ^{44}Ti synthesis is suppressed). We chose points along these tracks that exhibit identical peak densities and therefore have constant expansion timescales. Our aim here is not a full parameter survey of conditions relevant to ^{44}Ti synthesis, but rather an exploration of the sensitivity of ^{44}Ti synthesis to variations in crucial reaction rates affecting its production (and destruction) under conditions relevant to recent models and theory. Lacking detailed composition and velocity structure information our calculations cannot suggest firm predictions of ^{44}Ti synthesis for comparison to observation. Rather this limited survey will take a more general approach that could serve to place reasonable limits on the production of ^{44}Ti with respect to ^{56,57,58}Ni on the basis of nuclear systematics (Woosley et al. 1991).

Our results will be given in terms of normalized production factors (NPF) P_{44}, P_{57}, and P_{58}, that we define as the production factor for the given nucleus (the final mass fraction of the species in question divided by the mass fraction to which it decays in the Sun), normalized to the production factor for ^{56}Fe. Defined in this way NPF's for mass 56 (always made in these expansions predominantly as ^{56}Ni) are unity. Hence any NPF that is greater than unity will be overproduced with respect to solar iron, any NPF less than unity will be underproduced. Since roughly one-third to one-half of the iron in the Sun is attributable to SN II (Timmes, Woosley, & Weaver 1995), NPF's for radioactive ^{57,58}Ni up to a factor of $2-3$ would be acceptable (i.e. would not violate the solar ratio of ^{57}Fe/^{56}Fe). We consider these as upper bounds on the synthesis of ^{57,58}Ni. They also serve to illustrate the range of electron fraction (Y_e) allowed in such expansions. For reference, $X(^{44}\text{Ca})_\odot = 1.69 \times 10^{-6}$, $X(^{56}\text{Fe})_\odot = 1.26 \times 10^{-3}$, $X(^{57}\text{Fe})_\odot = 2.96 \times 10^{-5}$, $X(^{58}\text{Ni})_\odot = 5.52 \times 10^{-5}$ (Lodders 2003).

The decay of ^{56,57}Co (with half-lives of 77.2 and 271.7 days, respectively) powers the light curves of SN II after the initial hydrogen recombination phase until late times when the longer lived ^{44}Ti and ^{60}Co (with half-lives of 58.9 and 5.27 years, respectively) are expected to dominate (Timmes et al. 1996). Theory predicts that ^{44}Ti is always produced in much smaller amounts than ^{56,57}Ni, which we also infer from observations of Cassiopia A. This sets an upper bound on P_{44}. Of course it could always be less, especially if SN II are not the only source of ^{44}Ti.

4.2. ^{44}Ti Nucleosynthesis in Select Supernova Models

Before presenting our results we consider production of ^{44}Ti and ^{56,57,58}Ni from published models of SN II. The data are drawn from tables of stellar yields by Woosley et al. (1995), Rauscher et al. (2002), Limongi & Chieffi (2006), and Young et al. (2006). We calculate mass fractions by normalizing the radioactive yields (in $M_\odot$) to the total mass of material ejected (initial mass − mass loss − remnant mass) and then form the normalized production factor.

Figure 12 shows the NPF's for each nucleus versus initial stellar mass for $11 \leq M/M_\odot \leq 25$. We restrict our consideration to this mass range for two reasons: (1) for these solar metallicity models, the different treatments of mass loss are less pronounced for the lower masses, and (2) each survey explores a range of explosion energies for models with $M/M_\odot \geq 30$. Both can have a major impact on the ejected mass and the mass cut at higher masses. We do however show two results for the 25 $M_\odot$ model of Rauscher et al. (2002) where the explosion energy was increased to produce a model with double the yield of ^{56}Ni. We also

present results for a range of explosion energies in the 23 $M_\odot$ model of Young et al. (2006). The yields of Limongi & Chieffi (2006) were derived assuming a constant ^{56}Ni yield of 0.1 $M_\odot$.

For ^{57,58}Ni the results agree with the constraints imposed by the solar abundances, i.e. production factors between roughly 1 and 3 normalized to the production of ^{56}Fe in the Sun. The trends across the mass range shown, especially for ^{57}Ni, are quite similar, with the exception of the 20 $M_\odot$ model of Rauscher et al. (2002) that appears anomalous for reasons well described in that work.

For ^{44}Ti we see fairly remarkable consistency between the three large surveys for the masses between 18 and 25 $M_\odot$ with NPF's ranging between 0.1 and 0.2. Limongi & Chieffi (2006) never produce it above 0.1 for any mass, although its uniformity is in part due to the constant ^{56}Ni yield ejected. They are however very similar to those of Rauscher et al. (2002). Of note is the larger value for P_{44} in a 23 M$_\odot$ model of Cassiopia A (Young et al. 2006). The data reflect only their models with hydrogen envelopes removed to mimic a common-envelope evolution that also assumed a parameterized asymmetry of the explosion (those without asymetry ejected very little ^{56}Ni). The error bar reflects the variation of P_{44} due to their range of simulated explosion energies. A mixing algorithm was also included (absent in the other three surveys) whose role in the higher production of ^{44}Ti compared to the other surveys is unclear to us.

Even at a factor of 2 agreement this uniformity may seem surprising for models that have very different prescriptions for many important physics elements like mass loss (Woosley & Weaver had none), convection, opacities, and reaction rate libraries. Woosley et al. (1995) was the only one to not use as a base the Hauser-Feshbach reaction rate compilation of Rauscher & Thielemann (2000).

More important still for ^{44}Ti production is the parameterization of the explosion and determination of the mass cut. All three of the large surveys use a parameterization assuming motion of an inner zone (i.e., a piston approach) as opposed to thermal energy input (Thielemann, Nomoto, & Hashimoto 1996). Young et al. (2006) vary their explosion energies through a parameterization of flux-limited diffusion for neutrinos that includes a "trapping radius" at which the neutrino opacity and flux is artificially adjusted. It should be noted that all these efforts initiate the explosion and follow the nuclear burning and subsequent ejecta in one-dimension with the exception of Young et al. (2006) who, after 10-100 s, map their results from one-dimension to three-dimensions to follow the mixing and determine the ultimate ejecta distribution. Unfortunately, their nucleosynthesis results are preliminary and do not include results for ^{57,58}Ni, which should appear in a forthcoming work.

4.3. ^{44}Ti Nucleosynthesis Sensitivity Survey

We now consider results for each of our simulated expansions defined in Table 5. Figure 13 shows normalized production factors P_{44}, P_{57}, and P_{58} versus electron mole number Y_e for adiabatic freeze outs from peak conditions defined for points CasA $1-3$ in Table 5. All were drawn from a model for Cassiopia A (Magkotsios et al. 2008). In the figure, each central point represents a calculation that utilizes our recommended ^{40}Ca$(\alpha,\gamma)^{44}$Ti (production) rate for three choices of ^{44}Ti$(\alpha,p)^{47}$V (destruction) rate. Solid line type and filled squares represent our "recommended" destruction rate, filled triangles represent its upper (dotted) and lower (dashed) bound. The error bars on each central point for all three surveys reflect the minimum and maximum deviations of P_{44} due to the six other choices of the ^{40}Ca$(\alpha,\gamma)^{44}$Ti reaction rate that we considered. Tabulated nucleosynthesis results assuming our recommended semi-experimental production and destruction rates are given in Table 6.

The results for CasA points 1 and 2 are very similar. The NPF for ^{57}Ni and solar abundances suggest that the range of allowed electron fraction is $0.4980 \leq Y_e \leq 0.500$. As expected from nuclear systematics, in this range ^{44}Ti is always less (by mass fraction) than ^{57,58}Ni. It is also always underproduced with respect to solar iron ($P_{44} \leq P_{56} \equiv 1.0$). An increase in P_{44} is seen at lower Y_e, but this is due to a disparate drop in both ^{56}Ni and ^{44}Ti production (for point 2 between $Y_e = 0.49$ and 0.485, $(X^{56}\text{Ni})$ dropped by a factor of 46, while $(X^{44}\text{Ti})$ dropped by a factor of 3, respectively). For our "recommended" reaction rates the normalized production factors are very similar ($\sim 0.1 - 0.2$ over the entire allowed range of Y_e) to those seen in the SN II models with masses between 15 and 25 M$_\odot$ (Figure 12). For the lower bound on our destruction rate, they are a factor of 1.7 higher.

For point CasA-3 the results are very different. Now any choice of experimental rate for ^{40}Ca$(\alpha, \gamma)^{44}$Ti and either choice of our "recommended" or lower bound for the ^{44}Ti$(\alpha, p)^{47}$V destruction rate provides for nucleosynthesis that makes ^{44}Ti in proportion to solar iron over the allowed range of Y_e. Integrated results from a SN model that experiences these conditions in a sizable fraction of its ejecta would be of interest. Adopting our upper bound for ^{44}Ti$(\alpha, p)^{47}$V still makes P_{44} between 0.2 and 0.8, or up to double the value seen in the two older stellar model surveys. For Y_e less than 0.4980 the normalized production factors continue to climb but are suggesting a strong overproduction with respect to solar iron ($P_{57} \geq 3$, Table 6). For Y_e above 0.5, P_{44} is always small, even though the ^{56}Ni mass fraction remains high (~ 0.6). We also note that all three of these expansions were very α-rich (the final α-mass fractions across the Y_e range illustrated were 0.20, 0.23, and 0.32 for points CasA 1-3, respectively).

The contour plot of ^{44}Ti production in Magkotsios et al. (2008) suggests declining production for lower peak densities along the track of the CasA model. These translate to higher entropies (approaching 50 at $T_{9p} = 4.2$, $\rho_p = 5.0 \times 10^5$ g cm^{-3}), but the temperature is dropping so fast that NSE (needed to make ^{56}Ni) will be increasingly hard to achieve. For these peak conditions, assuming $Y_e = 0.498$ and our recommended principal production and destruction rates, the final α, ^{44}Ti, and ^{56,57,58}Ni mass fractions are 0.45, 1.8×10^{-3}, 0.38, 0.03, and 0.08 respectively, leading to NPF's $P_{44} = 3.53$, $P_{57} = 3.6$, and $P_{58} = 4.8$. This again suggests a strong overproduction of the later two with respect to solar iron.

For any given expansion the spread in values for P_{44} versus Y_e is straight forward to understand. In general, the value of Y_e tends to steer the net nuclear flows along pathways that are either proton-rich ($Y_e > 0.5$) or neutron-rich ($Y_e \leq 0.5$). Since ^{44}Ti and ^{56}Ni both have $Y_e = 0.5$, expansions of material that deviate far from this will reflect a drop in the abundance of each, although for ^{56}Ni, which is made in NSE, the change will be less dramatic, especially for proton-rich conditions (Seitenzahl et al. 2008). For all three points (CasA 1-3) the principle production rate affecting ^{44}Ti for all values of Y_e explored is ^{40}Ca$(\alpha, \gamma)^{44}$Ti. Differences in P_{44} across the range of Y_e surveyed are therefore driven principally by the reactions affecting the production of ^{40}Ca and the destruction of ^{44}Ti.

For $0.49 \leq Y_e \leq 0.5$ the dominant sequence of reactions producing ^{40}Ca are α-capture reactions on self-conjugate nuclei up to ^{36}Ar followed by ^{36}Ar$(\alpha, p)^{39}$K$(p, \gamma)^{40}$Ca, operating principally between $2 \leq T_9 \leq 3$. This is also true for $Y_e > 0.5$, but proton-induced (p, γ) and (p, α) flows provide additional pathways to build up ^{38}Ca at the expense of ^{40}Ca. Proton-capture reactions also compete strongly with ^{44}Ti$(\alpha, p)^{47}$V to accelerate the depletion of ^{44}Ti over the same temperature range. For $Y_e < 0.49$ proton-induced reactions that produce ^{40}Ca and destroy ^{44}Ti are suppressed due to the lower free proton abundance, the ones affecting production win out.

As mentioned above, the error bars on each point represent the variation in P_{44} due to the many choices of ^{40}Ca$(\alpha, \gamma)^{44}$Ti reaction rate we considered. For point CasA-3 this amounted to roughly 20% deviations

from our "recommended result", most often bracketed by our ×2 upper and lower error bar. Considering only the rates from other efforts, the variation would have been +20% and -10% from our recommended value. The variation is asymetric due to the relative ratios of the various production rates versus ours which was used to anchor the central point (see inset of Figure 9). If instead of the factor of 2 errors we assumed for the supplemental theory cross section we had used the errors suggested by our off-line counting data (Figure 4), the variation would have been of order 2%.

The choice of ^{44}Ti$(\alpha, p)^{47}$V destruction rate exhibits a larger sensitivity ($\sim 70\%$) to overall ^{44}Ti synthesis than the entire spread in the experimental ^{40}Ca$(\alpha, \gamma)^{44}$Ti production rates. Taken together, the potential uncertainty over the allowed Y_e range in ^{44}Ti synthesis encompassed by the possible choices of production and destruction rate is roughly a factor of 3.

Interestingly, the dot-short-dash lines in Figure 13 show ^{44}Ti synthesis considering the use of the original published fits (Rauscher & Thielemann 2000) for both ^{40}Ca$(\alpha, \gamma)^{44}$Ti and ^{44}Ti$(\alpha, p)^{47}$V, in very close agreement ($\sim 4\%$) with what resulted using our "recommended" rates. The reason is that for $1 \leq T_9 \leq 4$, the original fit to the production rate (Figure 9) made on average (more above $T_9 = 2.4$, less below) very nearly the same amount of ^{44}Ti as our "recommended rate", while the destruction rate (Figure 10) was nearly identical for $T_9 \geq 3$. Our higher production rate below $T_9 = 2.4$ accounted for the uniformly higher production. Again, this is the same level of variation from our recommended rate that would have occurred if we had considered only our offline counting error (Table 4). This would also be the result obtained using the default BDAT reaction rate library provided with the TORCH reaction network code (Timmes 2010, private communication), since it utilizes the same (original) fits to the relevant Hauser-Feshbach theory rates (Rauscher & Thielemann 2000) and 3α reaction rate (Caughlan & Fowler 1998).

Figure 14 shows our results for points 2DExpl $4-6$ (Table 6) drawn from conditions in a rotating two-dimensional SN explosion model. These have the same peak temperature albeit at higher peak density, as the points drawn from the CasA model, and sample the same regions as depicted in Magkotsios et al. (2008). The results for P_{57}, and P_{58} are very similar to those from the model for CasA (i.e. production compared to solar iron), but P_{44} is much smaller for all scenarios. It is similar however to that seen in the massive star surveys ($P_{44} \sim 0.1 - 0.2$, Figure 12). The final α-particle mass fractions across the Y_e range illustrated were roughly 0.10, 0.07, and 0.06 for points 4-6, respectively (Table 6).

According to Magkotsios et al. (2008) points 2DMHD $7-8$ represent conditions in a model for a rotating two-dimensional MHD star. Point 7 is located in the "Chasm" of ^{44}Ti production, while point 8 is in the region defined by them as incomplete silicon burning. Both experience much higher peak densities (at identical peak temperatures) than points from the previous two models, and consequently they have very low entropies and very short hydrodynamic time scales. Results assuming our "recommended" production and destruction rates are shown in Table 6. As before P_{57} and P_{58} are very similar to our previous results reflecting a near constant production of ^{57,58}Ni with respect to solar iron (for a given Y_e) over the entire range of expansion timescales surveyed. However, P_{44} was virtually non-existent, with $(X^{44}$Ti$) \leq 10^{-5}$ (often much less) for any Y_e in either expansion. Considering point 7, whose peak conditions reside in the "Chasm" of ^{44}Ti production noted in Magkotsios et al. (2008), our "recommended" reaction rates would slightly lessen (by 4%) the "depth" of the chasm compared to the reaction rates they used.

The explanation for the drop in P_{44} stems from the lower entropy (higher peak density) for each point in these rotating two-dimensional explosion model expansions versus those from the model for CasA (see Table 6). Similarly, for all three CasA points, the lower entropy expansions translated into a lower P_{44} (Figure 13). At lower entropy material merges very quickly into the iron group at the expense of the α-particle

abundance which at late times was so low ($\sim 1\%$) in the two-dimensional explosion model expansions that few were available to make ^{40}Ca at appreciable levels, with ^{44}Ti being consequently even lower.

From the track of the rotating two-dimensional explosion model we chose conditions (points 2DExpl $4-6$) that had identical peak densities, and hence a constant expansion timescale (0.14 s). For this factor of 2.6 overall change in entropy and for the specific case of $Y_e = 0.4980$, the final ^{56}Ni mass fractions were 0.74, 0.77, and 0.77 for points 2DExpl $4-6$, respectively. For the CasA model, with a factor of 1.5 range in entropy (that included a factor of 2 range of dynamic time-scale) the ^{56}Ni mass fractions were 0.64, 0.62, and 0.52 for points CasA 1-3, respectively. The salient point for ^{44}Ti synthesis again is that the higher entropy expansions made less ^{56}Ni and had more α-particles, especially at late times, that enabled the production of ^{40}Ca and ^{44}Ti (Table 6). Since P_{44} is a ratio of Ti to Fe, it grows as a function of increasing entropy.

We illustrate all these points graphically in Figure 15 where we show the evolution of select mass fractions versus temperature for the three expansions in our survey with identical peak temperatures (points 2, 5, and 8) that all started with an initial composition with $Y_e = 0.4980$. For each expansion both ^{40}Ca and ^{44}Ti achieve an NSE abundance not very different from their final freeze out values, but both are effectively destroyed for $4 \leq T_9 \leq 5$. Thereafter they are reassembled at a rate determined largely by the α-particle abundance, which is affected by the peak density (entropy). It is clear that a more robust α-rich freeze out is more conducive to ^{44}Ti synthesis and that reaction rates clearly matter.

We also note for all conditions shown in Figure 15 the freeze-out of the ^{44}Ti abundance near $T_9 = 2$. The ^{47}V abundance does increase as the temperature declines, but the ^{44}Ti abundance changes by less than a few percent (the increase is due predominantly to the decay of radioactive ^{47}Cr). At this Y_e and for $T_9 \geq 2.0$ the dominant destruction rate for ^{44}Ti is ^{44}Ti$(\alpha, p)^{47}$V, below 1.0 it switches to ^{44}Ti$(p, \gamma)^{45}$V. Terminating our simulations at any point below $T_9 = 2.0$ would have a negligible effect on P_{44}.

4.3.1. Effect of the Expansion Timescale

^{44}Ti synthesis is also affected by the expansion timescale, $\tau_{\mathrm{HD}} = 446\chi/\sqrt{\rho_p}$. Figure 16 shows the range of nuclei produced in an α-rich freeze-out from peak conditions given for point CasA-3 in Table 5 with an initial composition of $Y_e = 0.4980$ and our default scaling of $\chi = 1$. The nucleosynthesis is presented in terms of "traditional" production factors (so far our results have been expressed as ratios of production factors to that of ^{56}Fe). In the figure isotopes of a given element are connected by solid lines, those produced as radioactive progenitors are surrounded by a diamond, the most abundant isotope of a given element is denoted by a star. The dotted lines indicate a factor of 2 above and below the dashed line centered on ^{56}Fe (made as ^{56}Ni, ^{44}Ca is made as ^{44}Ti). The dominant species are in the iron group. This is a fairly typical result for any of the CasA or two-dimensional explosion model expansions within the allowed range of Y_e.

Figure 17 explores the effect of increasing the hydrodynamic time-scale by a factor of $\chi = 5$. Shown is a straight forward ratio of "traditional" production factors for the CasA-3 expansion assuming both the default ($\chi = 1$) and extended ($\chi = 5$) scaling on τ_{HD}. The species in the iron group are not much affected, ^{56,58}Ni are slightly higher than unity, all others show lower production factors. The reason is that for a longer expansion timescale, the material experiences higher temperatures for a longer duration. Those made dominantly in NSE (the iron group seen here) are slightly altered due to α-particle reactions on them, which are ultimately provided by photo-disintegration and operation of the 3α-reaction. The effect is to reduce the overall fraction of α-particles available at late times for the re-assembly of species lighter than the iron group.

Figure 18 shows for the specific CasA-3 example above the temperature evolution over the first 4 s assuming the two scalings. Over that time the temperature in the default ($\chi = 1$, dotted line) scenario declined from $T_9 = 4.7$ - 0.25 while the longer expansion ($\chi = 5$, dashed line) only declined to $T_9 = 2.6$. Also shown is the ratio of the α-particle mass fraction (long/default). Recall that both ^{40}Ca and ^{44}Ti begin to re-assemble below $T_9 = 4$ (Figure 15). By the time the longer expansion scenario reaches $T_9 = 4$, it only has 65% of the α-particle mass fraction that the default expansion had, by $T_9 = 3$ it is down to 52%. With only half the α-particles to work with, the expansion with the higher scaling only reached $P_{44} = 0.5 \pm 0.1$, a factor of 2.6 less than the default expansion. Figure 19 shows the effect over all scenarios considered in the CasA model expansions. The average P_{44} for points 4-6 (the two-dimensional explosion model) were 0.1, 0.05, and 0.08, respectively, over the allowed range of Y_e. For points 7 and 8 they are essentially zero.

5. Conclusions

We have considered the sensitivity to ^{44}Ti production in expansions that approximate freeze outs from NSE due to variations in the principle production and destruction reactions ^{40}Ca$(\alpha, \gamma)^{44}$Ti and ^{44}Ti$(\alpha, p)^{47}$V, and contrast them to experimental and theory reaction rate developments over the past 20 years. Experimentally we have also measured a thick-target yield for the ^{40}Ca$(\alpha,\gamma)^{44}$Ti reaction. In-beam γ-ray spectroscopy was used to determine the yield of the 1083 keV prompt γ-ray from ^{44}Ti at $E_\alpha = 4.13$, 4.54, and 5.36 MeV. In order to correct for those transitions which bypass the 1083 keV transition, the Monte Carlo code DICEBOX was used to estimate a correction of 20% to the in-beam thick target yield. An off-line activation measurement using the target from the $E_\alpha = 5.36$ MeV irradiation showed good agreement with the in-beam measurement.

We then derived a thermonuclear reaction rate by normalizing the NON-SMOKER cross section (down by a factor of 1.71) to agree with our measured off-line thick target yield. We derived an error bar for our recommended rate whose magnitude ($\pm \times 2$) was dominated by the *theoretical* cross section error. We also carry out a similar re-evaluation of the ^{44}Ti$(\alpha, p)^{47}$V reaction rate whose cross section was measured by Sonzogni et al. (2000). For both reactions, we conclude that the experimental data were far above the Gamow window, and suggest that further measurements be attempted.

We then carried out a sensitivity survey of ^{44}Ti nucleosynthesis in adiabatic expansions from eight peak temperature and density combinations drawn from conditions in three recent stellar explosion models (Magkotsios et al. 2008). For each expansion we survey a range of initial compositions ($0.505 \geq Y_e \geq 0.485$). We also vary the principle production and destruction rates affecting ^{44}Ti in these expansions (eight choices of production rate, four for destruction). Our results show ^{44}Ti produced in proportion to solar iron for only one expansion drawn from a model for Cassiopia A, even though the final mass fractions for ^{44}Ti in most of the expansions are typically of order 10^{-4}. With one exception, the other expansions are consistent with ^{44}Ti production seen in previous surveys of one-dimensional stellar evolution and with constraints imposed by solar abundances. Our results suggest that a strong α-rich freeze out ($(X(\alpha)_f \sim 0.2 - 0.3$) is highly conducive to ^{44}Ti synthesis.

With respect to reaction rate sensitivity, our experimental results suggest a recommended ^{40}Ca$(\alpha, \gamma)^{44}$Ti reaction rate that is smaller than those predicted by the most recent experimental efforts (Vockenhuber et al. 2007; Nassar et al. 2006), but with a fairly large error bar ($\pm \times 2$) that would in fact encompass the former one. Nucleosynthesis models using our recommended rate would suggest less ^{44}Ti than these two recent experiments, although it would be higher than that suggested by an earlier measured rate (Cooperman et al.

1977) and the current theory rate (Rauscher & Thielemann 2000). The total range of sensitivity is a factor of 1.5 (36%) when considering all of the production rates available. We also find that the uncertainties associated with the dominant destruction rate, $^{44}\text{Ti}(\alpha, p)^{47}\text{V}$, have roughly double the impact on ^{44}Ti synthesis ($\times 3.2$, or 70%) than that exhibited by the entire range of production rates. We suggest the use of our re-evaluation of the only available experimental reaction rate (Sonzogni et al. 2000) and strongly suggest consideration of its attendant larger uncertainty ($\pm \times 3$). This is a slightly larger spread in ^{44}Ti sensitivity than observed in two recent surveys of massive star nucleosynthesis (Rauscher et al. 2002; Limongi & Chieffi 2006) that used essentially the same nuclear data, suggesting that current uncertainties in reaction rates could lead to as large an uncertainty in ^{44}Ti synthesis as that produced by different treatments of stellar physics.

Since the seminal work of Woosley et al. (1973), several new and novel theories of SN nucleosynthesis have featured regimes within the neutrino wind where the $\alpha-$rich freeze out plays an important role, including scenarios for the r-process (Woosley et al. 1994; Hoffman et al. 1997), and the νp-process (Fröhlich et. al. 2006; Pruet et. al. 2006). In each a combination of high entropy ($S_{\text{rad}} \geq 50$) and short expansion time-scale are required to produce the unique signatures of each process (the r-abundances, and light p-nuclei, respectively). However, as a consequence of extreme neutrino irradiation, the composition is forced away from neutron-proton equality and ultimately high entropy material enters regions above the iron group where local effects due to rapid changes in particle separation energies have a strong influence on the net nuclear flows. In these works no ^{44}Ti is reported.

Further out in the SN ejecta theory does not show ^{44}Ti enhancement due to the ν-process in massive stars (Woosley et al. 1990; Woosley et al. 1995), nor in recent low-mass (electron capture) core-collapse scenarios (Hoffman et al. 2008; Wanajo et al. 2009). The later has been shown to effectively synthesize the long elusive α-rich freeze-out candidate ^{64}Zn, but not ^{44}Ti. Our limited survey suggests that ^{44}Ti synthesis requires modest entropy ($S_{\text{rad}} \sim 35$) and expansion timescales ($\sim \tau_{\text{HD}} = 0.45$ s) over a fairly narrow range of Y_e ($0.5 \geq Y_e \geq 0.4980$).

To date surveys of massive star evolution and nucleosynthesis have typically underproduced species whose production is attributed to the α-rich freeze-out, in particular ^{44}Ca (made as ^{44}Ti) and ^{64}Zn (Woosley et al. 1995; Limongi & Chieffi 2006). This has largely been ascribed to variations in treatments of stellar physics, most notably the parameterization of the explosion in one-dimensional models. Incorporating stellar yields from these surveys into models for galactic chemical evolution indicate the degree of underproduction, roughly a factor of a $2-3$ (Timmes, Woosley, & Weaver 1995). Recent work has lead to models for the progenitor of Cassiopia A that suggest increased production, but the underlying physics is still quite uncertain and in need of improvement (Young et al. 2006). Future attention may focus on issues related to *asymmetrical* explosions where a noted increase in ^{44}Ti production compared to models with imposed spherical symmetry has been suggested for many years (Nagataki et al. 1997; Nagataki et al. 1998; Hwang & Laming 2003; Young et al. 2006). The community is on the threshold of three-dimensional calculations that should provide valuable insight into the core-collapse mechanism, including physics such as rotation and magnetic fields which will likely enforce an asymmetrical result. Such results should help guide future parameterizations of the explosion in our one-dimensional models which will continue to carry the burden in future surveys of massive star evolution and nucleosynthesis. We believe we have addressed the uncertainty in two key nuclear reaction rates affecting ^{44}Ti synthesis, but ultimately, if Type II SNe are the dominant site of ^{44}Ti production, future models will have to include a larger fraction of their ejecta that experience an α-rich freeze out than they have in the past. Another solution would be an additional source of ^{44}Ti, such as rare SNe of type Ia (Woosley et al. 1986; Woosley 1997) or Ib (Perets et al. 2010).

REFERENCES

Ahmad, I. et al. 2006, Phys. Rev., C74, 065802

Becvar, F. 1998, Nucl. Instrum. Methods Phys. Res. A, 471, 434 (DICEBOX)

Caughlan, G. R., & Fowler, W. A. 1988, At. Data Nucl. Data Tables, 40, 283

Clayton, D. D. 1984, Principles of Stellar Evolution and Nucleosynthesis (Univ. Chicago Press) Chicago, London

Cooperman, E. et al. 1977, Nucl. Phys., A284, 284

Czosnyka, T. et al. 1983, Am. Phys. Soc., 28, 745

Diehl, R. et al. 2006, Nucl. Phys., A777, 70

Dyer, P. et al. 1981, Phys. Rev., C23, 1865

Fisker, J. L. *et. al.* 2001, At. Data Nucl. Data Tables, 79, 241

Fowler, W. A., Caughlan, G. R., & Zimmerman, B. A. 1967, ARA&A, 5, 525

Fröhlich, C., Martínez-Pinedo, G., Liebendörfer, M., Thielemann, F.-K., Bravo, E., Hix, W. R., Langanke, K.-H., & Zinner, N. T. 2006, Phys. Rev. Lett. 96, 142502

Gete, E. et al. 1997, Nucl. Instrum. Methods Phys. Res. A, 388, 212

Hartmann, D., Woosley, S. E., & El Eid, M. F. 1985, ApJ, 297, 837

Hoffman, R. D., Woosley, S. E., & Qian, Y.-Z. 1997, ApJ, 482, 951

Hoffman, R. D. et al. 2002, RateTable v. 8.2, http://adg.llnl.gov/Research/RRSN/

Hoffman, R. D., Muller, B, & Janka, H. T. 2008, ApJ, L676, 127

Holmes, J. A. et al. 1976, At. Data Nucl. Data Tables, 18, 306

Hsu, H. H. 1982, Nucl. Instrum. Methods, 193, 383

Hwang, U., & Laming, J. M. 2003, ApJ, 597, 362

Iliadis, C. 2007, Nuclear Physics of Stars (Wiley-VCH), Berlin

Iyudin, A. F. et al. 1994, A&A, 284, L1

—. 1998, Nature, 396, 142

Kiss, G. G., Rauscher, T., Gyürky, Gy., Simon, A., Fülöp, Zs., & Somorjai, E. 2008, Phys. Rev. Lett. 101, 191101

Limongi, M. & Chieffi, A. 2006, ApJ, 647, 483

Lodders, K. 2003, ApJ, 591, 1220

Magkotsios, G. L. et al. 2008, in Proc. 10th Symp. Nuclei in the Cosmos (NIC X), 112

Nagataki, S., Hashimoto, M.-A., Sato, K., & Yamada, S. 1997, ApJ, 486, 1026

Nagataki, S., Hashimoto, M.-A., Sato, K., Yamada, S., & Mochizuki, Y. S. 1998, ApJ, 492, L45

Nassar, H. et al. 2006, Phys. Rev. Lett., 96, 041102

Perets, H. B. et. al. 2010, Nature, in press, http://adsabs.harvard.edu/abs/2009arXiv0906.2003P

Pruet, J., Hoffman, R. D., Woosley, S. E., Janka, H.-T., & Buras, R., 2006, ApJ, 644, 1028

Rauscher, T. 2010, Phys. Rev. C, 81, 4, http://link.aps.org/doi/10.1103/PhysRevC.81.045807

Rauscher, T. 2003-2009, Code EXP2RATE, http://download.nucastro.org/codes/exp2rate.f

Rauscher, T. & Thielemann, F. 2001, At. Data Nucl. Data Tables, 75, 1

—. 2001, At. Data Nucl. Data Tables, 79, 47

Rauscher, T. et al. 2000, Nucl. Phys., A675, 695

Rauscher, T. et al. 2002, ApJ, 576, 323

Rauscher, T. et al. 2009, Phys. Rev., C80, 035801

Renaud, M. et al. 2006, ApJ, 647, L41

Roughton, N. A., Fritts, M. J., Peterson, R. J., Zaidins, C. S., and Hansen, C. J. 1976, ApJ, 205, 302

Seitenzahl, I. R., Timmes, F. X., Marin-Lafleche, A., Brown, E., Magkotsios, G., and Truran, J. 2008, ApJ, 685L, 129S

Simpson, J. et al. 1971, Phys. Rev., C4, 443

Sonzogni, A. A. et al. 2000, Phys. Rev. Lett., 84, 1651

The, L. S. et al. 1998, ApJ, 504, 500

The, L.-S. et al. 2006, A&A, 450, 1037

Thielemann, F.-K., Arnould, M., & Truran, J. 1987, in Advances in Nuclear Astrophysics, ed. E. Vangioni-Flam (Gif-sur-Yvette: Editions Frontiere), 525

Thielemann, F.-K., Nomoto, K., & Hashimoto, M. 1996, ApJ, 460, 408

Timmes, F. X., Woosley, S. E., and Weaver, T. A. 1995, ApJS, 98, 617

Timmes, F. et al. 1996, ApJ, 464, 332

Timmes, F., private communication, see also http://cococubed.asu.edu/code_pages/net_torch.shtml

Vink, J. et al. 2001, ApJ, 560, L79

Vockenhuber, C. et al. 2007, Phys. Rev., C76, 035801

Wanajo, S. et al. (2009), ApJ, 695, 208

Woosley, S. E. 1997, ApJ, 476, 801

Woosley, S. E., Taam, R. E., & Weaver, T. A. 1986, ApJ, 301, 601

Woosley, S. E., Arnett, D., & Clayton, D.D. 1973, ApJS, 26, 231

Woosley, S. E., Fowler, W. A., Holmes, J. A., & Zimmerman, B. A. 1978, Atomic Data & Nuclear Data Tables, 22, 371 - (see also "Tables of Thermonuclear Reaction Rate Data for Intermediate Mass Nuclei", OAP-422, (Caltech preprint, August 1975)

Woosley, S. E., Hartmann, D. H., Hoffman, R. D., & Haxton, W. C. 1990, ApJ, 365, 272

Woosley, S. E. & Hoffman, R. D. 1991, ApJ, 368, L31

Woosley, S. E., Wilson, J. R., Mathews G. J., Hoffman, R. D., & Meyer, B. S. 1994, ApJ, 433, 209

Woosley, S. E., & Weaver, T. 1995, ApJS, 101, 181

Young, P. A. et al. 2006, ApJ, 640, 891

Ziegler, J. F. 2004, Nucl. Instrum. Methods B, 219, 1027

Table 6. Nucleosynthesis Survey[1]

Y_e	0.5050	0.5000	0.4995	0.4990	0.4985	0.4980	0.4965	0.4950	0.4900	0.4850
η	-0.0100	0.0000	0.0010	0.0020	0.0030	0.0040	0.0070	0.0100	0.0200	0.0300
Point 1: Model for Cassiopia A, $T_{9p} = 6.5$, $\rho_p = 4.0 \times 10^6$, $S_{\rm rad} = 22.8$, $\tau_{\rm HD} = 0.22$ s										
$X(\alpha)$	2.06(-1)	2.08(-1)	2.07(-1)	2.06(-1)	2.04(-1)	2.03(-1)	1.98(-1)	1.94(-1)	1.79(-1)	1.64(-1)
$X(^{40}\rm Ca)$	1.66(-4)	8.27(-4)	7.87(-4)	7.46(-4)	7.15(-4)	6.89(-4)	6.26(-4)	5.72(-4)	4.25(-4)	1.00(-4)
$X(^{44}\rm Ti)$	6.17(-5)	3.00(-4)	3.49(-4)	3.42(-4)	3.34(-4)	3.27(-4)	3.05(-4)	2.85(-4)	2.22(-4)	7.39(-5)
$X(^{56}\rm Ni)$	7.51(-1)	7.35(-1)	7.17(-1)	6.92(-1)	6.66(-1)	6.39(-1)	5.58(-1)	4.77(-1)	2.11(-1)	4.58(-3)
$X(^{57}\rm Ni)$	2.09(-3)	1.22(-2)	2.89(-2)	3.09(-2)	3.27(-2)	3.42(-2)	3.78(-2)	3.98(-2)	3.48(-2)	4.52(-3)
$X(^{58}\rm Ni)$	2.25(-5)	1.57(-3)	9.70(-3)	3.50(-2)	6.04(-2)	8.59(-2)	1.63(-1)	2.41(-1)	5.08(-1)	6.97(-1)
P_{44}	0.062	0.305	0.364	0.369	0.374	0.382	0.409	0.446	0.786	12.027
P_{57}	0.131	0.707	1.717	1.891	2.079	2.283	2.889	3.536	7.024	42.192
P_{58}	0.004	0.221	0.309	1.153	2.060	3.071	6.659	11.504	54.762	3452.055
Point 2: Model for Cassiopia A, $T_{9p} = 5.5$, $\rho_p = 2.0 \times 10^6$, $S_{\rm rad} = 27.7$, $\tau_{\rm HD} = 0.32$ s										
$X(\alpha)$	2.22(-1)	2.25(-1)	2.25(-1)	2.23(-1)	2.22(-1)	2.21(-1)	2.16(-1)	2.12(-1)	1.98(-1)	1.84(-1)
$X(^{40}\rm Ca)$	2.47(-4)	9.50(-4)	9.06(-4)	8.61(-4)	8.27(-4)	7.99(-4)	7.30(-4)	6.73(-4)	5.15(-4)	1.04(-4)
$X(^{44}\rm Ti)$	8.66(-5)	3.59(-4)	4.14(-4)	4.06(-4)	3.98(-4)	3.90(-4)	3.68(-4)	3.46(-4)	2.80(-4)	8.13(-5)
$X(^{56}\rm Ni)$	7.35(-1)	7.17(-1)	6.99(-1)	6.75(-1)	6.48(-1)	6.22(-1)	5.40(-1)	4.59(-1)	1.92(-1)	3.06(-3)
$X(^{57}\rm Ni)$	2.18(-3)	1.22(-2)	2.82(-2)	3.00(-2)	3.17(-2)	3.32(-2)	3.65(-2)	3.82(-2)	3.25(-2)	3.17(-3)
$X(^{58}\rm Ni)$	2.53(-5)	2.03(-3)	1.00(-2)	3.54(-2)	6.09(-2)	8.64(-2)	1.64(-1)	2.42(-1)	5.09(-1)	6.57(-1)
P_{44}	0.088	0.374	0.441	0.450	0.458	0.468	0.508	0.562	1.085	19.836
P_{57}	0.132	0.721	1.715	1.884	2.078	2.267	2.867	3.534	7.190	44.672
P_{58}	0.004	0.216	0.328	1.198	2.136	3.178	6.900	12.000	60.261	4877.049
Point 3: Model for Cassiopia A, $T_{9p} = 4.7$, $\rho_p = 1.0 \times 10^6$, $S_{\rm rad} = 34.5$, $\tau_{\rm HD} = 0.45$ s										
$X(\alpha)$	3.13(-1)	3.17(-1)	3.16(-1)	3.15(-1)	3.14(-1)	3.13(-1)	3.09(-1)	3.06(-1)	2.96(-1)	2.86(-1)
$X(^{40}\rm Ca)$	7.70(-4)	2.10(-3)	2.04(-3)	1.94(-3)	1.87(-3)	1.82(-3)	1.69(-3)	1.59(-3)	1.31(-3)	1.85(-4)
$X(^{44}\rm Ti)$	2.05(-4)	8.57(-4)	9.81(-4)	9.69(-4)	9.57(-4)	9.45(-4)	9.10(-4)	8.77(-4)	7.74(-4)	1.44(-4)
$X(^{56}\rm Ni)$	6.40(-1)	6.17(-1)	5.99(-1)	5.75(-1)	5.49(-1)	5.22(-1)	4.41(-1)	3.60(-1)	9.43(-2)	2.56(-3)
$X(^{57}\rm Ni)$	1.83(-3)	1.27(-2)	2.81(-2)	2.99(-2)	3.15(-2)	3.29(-2)	3.55(-2)	3.62(-2)	2.39(-2)	1.30(-3)
$X(^{58}\rm Ni)$	2.21(-5)	2.56(-3)	8.26(-3)	3.29(-2)	5.77(-2)	8.26(-2)	1.58(-1)	2.34(-1)	4.94(-1)	4.31(-1)
P_{44}	0.238	1.037	1.223	1.258	1.300	1.349	1.543	1.818	6.120	41.053
P_{57}	0.123	0.878	1.994	2.210	2.454	2.675	3.429	4.266	10.787	22.010
P_{58}	0.003	0.243	0.315	1.304	2.408	3.614	8.171	14.825	119.333	3732.058
Point 4: Rotating Two-dimensional Explosion Model, $T_{9p} = 6.5$, $\rho_p = 1.0 \times 10^7$, $S_{\rm rad} = 9.14$, $\tau_{\rm HD} = 0.14$ s										
$X(\alpha)$	1.03(-1)	1.06(-1)	1.05(-1)	1.04(-1)	1.03(-1)	1.02(-1)	9.77(-2)	9.39(-2)	8.14(-2)	6.95(-2)
$X(^{40}\rm Ca)$	2.00(-5)	4.54(-4)	4.32(-4)	4.03(-4)	3.81(-4)	3.62(-4)	3.15(-4)	2.75(-4)	1.74(-4)	8.54(-5)
$X(^{44}\rm Ti)$	3.11(-5)	1.34(-4)	1.90(-4)	1.83(-4)	1.77(-4)	1.70(-4)	1.51(-4)	1.34(-4)	8.76(-5)	4.87(-5)
$X(^{56}\rm Ni)$	8.50(-1)	8.40(-1)	8.21(-1)	7.94(-1)	7.67(-1)	7.39(-1)	6.56(-1)	5.74(-1)	3.04(-1)	4.68(-2)
$X(^{57}\rm Ni)$	4.15(-3)	1.13(-2)	2.79(-2)	3.07(-2)	3.32(-2)	3.55(-2)	4.07(-2)	4.40(-2)	4.30(-2)	1.98(-2)
$X(^{58}\rm Ni)$	7.02(-5)	9.96(-4)	1.14(-2)	3.58(-2)	6.04(-2)	8.51(-2)	1.60(-1)	2.37(-1)	5.03(-1)	7.79(-1)
P_{44}	0.029	0.119	0.173	0.173	0.172	0.172	0.172	0.175	0.216	0.777
P_{57}	0.267	0.571	1.445	1.648	1.839	2.044	2.649	3.268	6.017	18.011
P_{58}	0.021	0.183	0.317	1.029	1.790	2.624	5.566	9.408	37.801	379.032

[1] All results assume our "recommended" rates for $^{40}\rm Ca(\alpha,\gamma)^{44}Ti$ and $^{44}\rm Ti(\alpha,p)^{47}V$.

Table 6. Nucleosynthesis Survey[1] (*continued*)

Y_e	0.5050	0.5000	0.4995	0.4990	0.4985	0.4980	0.4965	0.4950	0.4900	0.4850
η	-0.0100	0.0000	0.0010	0.0020	0.0030	0.0040	0.0070	0.0100	0.0200	0.0300
Point 5: Rotating Two-dimensional Explosion Model, $T_{9p} = 5.5$, $\rho_p = 1.0 \times 10^7$, $S_{rad} = 5.54$, $\tau_{HD} = 0.14$ s										
$X(\alpha)$	6.85(-2)	7.23(-2)	7.17(-2)	7.07(-2)	6.96(-2)	6.85(-2)	6.53(-2)	6.21(-2)	5.23(-2)	4.36(-2)
$X(^{40}\text{Ca})$	1.13(-5)	3.68(-4)	3.56(-4)	3.29(-4)	3.08(-4)	2.90(-4)	2.46(-4)	2.10(-4)	1.23(-4)	6.11(-5)
$X(^{44}\text{Ti})$	1.61(-5)	8.16(-5)	1.62(-4)	1.54(-4)	1.47(-4)	1.41(-4)	1.22(-4)	1.05(-4)	6.34(-5)	3.43(-5)
$X(^{56}\text{Ni})$	8.77(-1)	8.74(-1)	8.54(-1)	8.27(-1)	7.99(-1)	7.71(-1)	6.87(-1)	6.04(-1)	3.31(-1)	6.85(-2)
$X(^{57}\text{Ni})$	7.18(-3)	9.75(-3)	2.59(-2)	2.92(-2)	3.22(-2)	3.48(-2)	4.08(-2)	4.45(-2)	4.47(-2)	2.40(-2)
$X(^{58}\text{Ni})$	1.86(-4)	8.99(-4)	1.18(-2)	3.54(-2)	5.92(-2)	8.33(-2)	1.57(-1)	2.32(-1)	4.95(-1)	7.73(-1)
P_{44}	0.015	0.070	0.142	0.139	0.137	0.136	0.132	0.130	0.143	0.373
P_{57}	0.451	0.474	1.291	1.502	1.717	1.928	2.527	3.125	5.741	14.926
P_{58}	0.056	0.157	0.316	0.977	1.685	2.467	5.201	8.771	34.144	257.353
Point 6: Rotating Two-dimensional Explosion Model, $T_{9p} = 4.7$, $\rho_p = 1.0 \times 10^7$, $S_{rad} = 3.45$, $\tau_{HD} = 0.14$ s										
$X(\alpha)$	5.67(-2)	6.07(-2)	6.04(-2)	5.97(-2)	5.90(-2)	5.84(-2)	5.65(-2)	5.48(-2)	4.99(-2)	4.58(-2)
$X(^{40}\text{Ca})$	1.36(-5)	4.91(-4)	5.04(-4)	4.67(-4)	4.42(-4)	4.20(-4)	3.71(-4)	3.32(-4)	2.36(-4)	1.46(-4)
$X(^{44}\text{Ti})$	1.19(-5)	6.90(-5)	2.42(-4)	2.33(-4)	2.24(-4)	2.17(-4)	1.96(-4)	1.79(-4)	1.34(-4)	9.15(-5)
$X(^{56}\text{Ni})$	8.68(-1)	8.76(-1)	8.56(-1)	8.28(-1)	7.99(-1)	7.71(-1)	6.86(-1)	6.02(-1)	3.26(-1)	6.19(-2)
$X(^{57}\text{Ni})$	1.14(-2)	8.83(-3)	2.47(-2)	2.85(-2)	3.18(-2)	3.46(-2)	4.09(-2)	4.46(-2)	4.42(-2)	2.28(-2)
$X(^{58}\text{Ni})$	4.46(-4)	8.06(-4)	1.05(-2)	3.22(-2)	5.43(-2)	7.66(-2)	1.45(-1)	2.15(-1)	4.59(-1)	7.14(-1)
P_{44}	0.011	0.059	0.210	0.210	0.209	0.209	0.213	0.222	0.306	1.102
P_{57}	0.720	0.428	1.229	1.464	1.685	1.912	2.532	3.159	5.753	15.650
P_{58}	0.139	0.143	0.281	0.888	1.550	2.271	4.826	8.159	32.124	262.195
Point 7: Rotating Two-dimensional MHD Model (CHASM region), $T_{9p} = 6.5$, $\rho_p = 1.0 \times 10^8$, $S_{rad} = 0.91$, $\tau_{HD} = 0.04$ s										
$X(\alpha)$	1.01(-2)	1.31(-2)	1.20(-2)	1.08(-2)	9.65(-3)	8.51(-3)	5.25(-3)	2.26(-3)	1.81(-6)	8.95(-7)
$X(^{40}\text{Ca})$	7.43(-8)	3.61(-5)	2.64(-5)	1.94(-5)	1.41(-5)	9.95(-6)	2.68(-6)	2.88(-7)	4.06(-8)	2.35(-7)
$X(^{44}\text{Ti})$	1.22(-7)	1.15(-5)	1.11(-5)	8.25(-6)	5.97(-6)	4.19(-6)	1.08(-6)	1.06(-7)	1.98(-9)	6.31(-9)
$X(^{56}\text{Ni})$	8.67(-1)	9.40(-1)	9.14(-1)	8.87(-1)	8.59(-1)	8.32(-1)	7.52(-1)	6.71(-1)	3.93(-1)	1.28(-1)
$X(^{57}\text{Ni})$	1.06(-2)	1.34(-2)	2.30(-2)	2.84(-2)	3.30(-2)	3.69(-2)	4.57(-2)	5.15(-2)	4.88(-2)	3.07(-2)
$X(^{58}\text{Ni})$	7.53(-4)	1.50(-4)	1.92(-2)	4.21(-2)	6.61(-2)	9.11(-2)	1.72(-1)	2.60(-1)	4.30(-1)	5.61(-1)
P_{44}	0.000	0.009	0.009	0.007	0.005	0.004	0.001	0.000	0.000	0.000
P_{57}	1.327	0.607	1.069	1.365	1.642	1.891	2.596	3.265	5.272	10.388
P_{58}	1.244	0.064	0.478	1.082	1.760	2.496	5.209	8.837	24.888	99.029
Point 8: Rotating Two-dimensional MHD Model, $T_{9p} = 5.5$, $\rho_p = 1.0 \times 10^8$, $S_{rad} = 0.55$, $\tau_{HD} = 0.04$ s										
$X(\alpha)$	9.27(-3)	1.13(-2)	1.07(-2)	9.89(-3)	9.16(-3)	8.47(-3)	6.57(-3)	4.86(-3)	4.69(-4)	2.45(-6)
$X(^{40}\text{Ca})$	1.39(-7)	5.28(-5)	4.50(-5)	3.56(-5)	2.84(-5)	2.27(-5)	1.12(-5)	4.92(-6)	1.59(-8)	4.70(-10)
$X(^{44}\text{Ti})$	2.14(-7)	6.95(-6)	2.06(-5)	1.65(-5)	1.33(-5)	1.07(-5)	5.20(-6)	2.24(-6)	5.93(-9)	4.65(-11)
$X(^{56}\text{Ni})$	7.86(-1)	9.25(-1)	9.01(-1)	8.74(-1)	8.47(-1)	8.20(-1)	7.39(-1)	6.59(-1)	3.89(-1)	1.18(-1)
$X(^{57}\text{Ni})$	1.07(-2)	8.79(-3)	2.10(-2)	2.67(-2)	3.14(-2)	3.52(-2)	4.39(-2)	4.95(-2)	5.37(-2)	3.37(-2)
$X(^{58}\text{Ni})$	1.40(-3)	2.13(-4)	1.47(-2)	3.50(-2)	5.64(-2)	7.89(-2)	1.52(-1)	2.32(-1)	5.45(-1)	7.60(-1)
P_{44}	0.000	0.006	0.017	0.014	0.012	0.010	0.005	0.003	0.000	0.000
P_{57}	1.505	0.404	0.992	1.298	1.575	1.828	2.521	3.193	5.890	12.301
P_{58}	2.660	0.086	0.373	0.914	1.516	2.197	4.685	8.031	31.974	146.341

[1] All results assume our "recommended" rates for $^{40}\text{Ca}(\alpha,\gamma)^{44}\text{Ti}$ and $^{44}\text{Ti}(\alpha,p)^{47}\text{V}$.
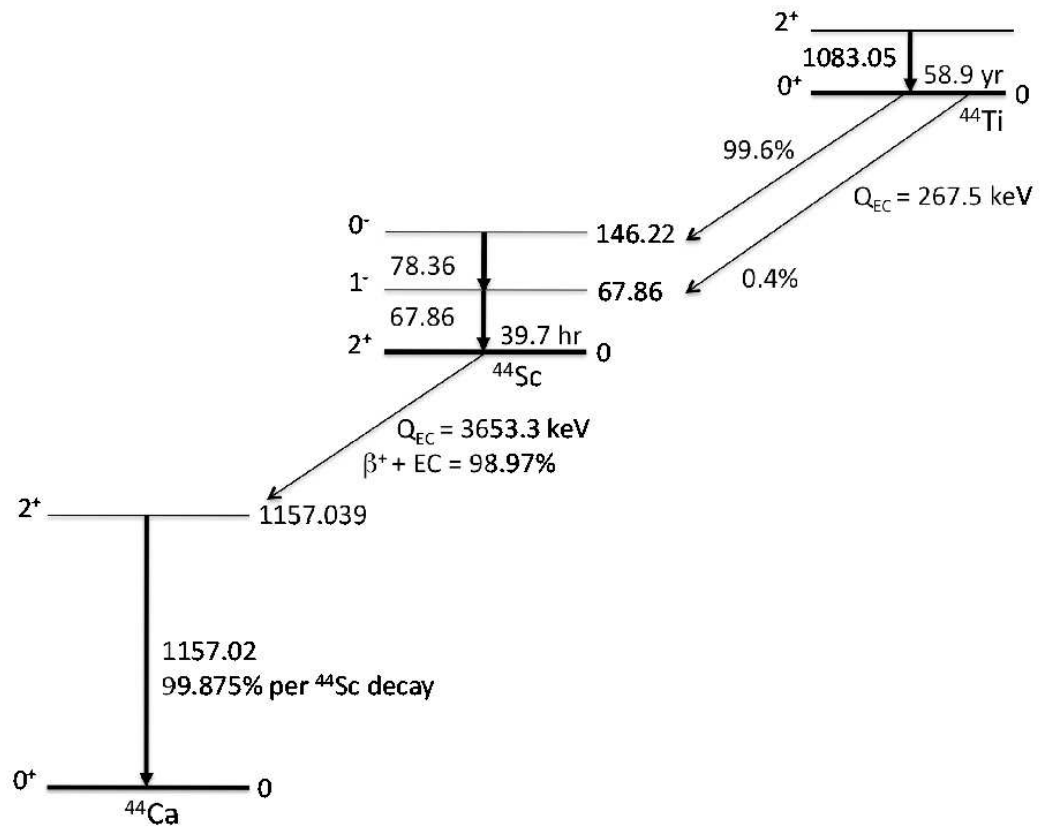
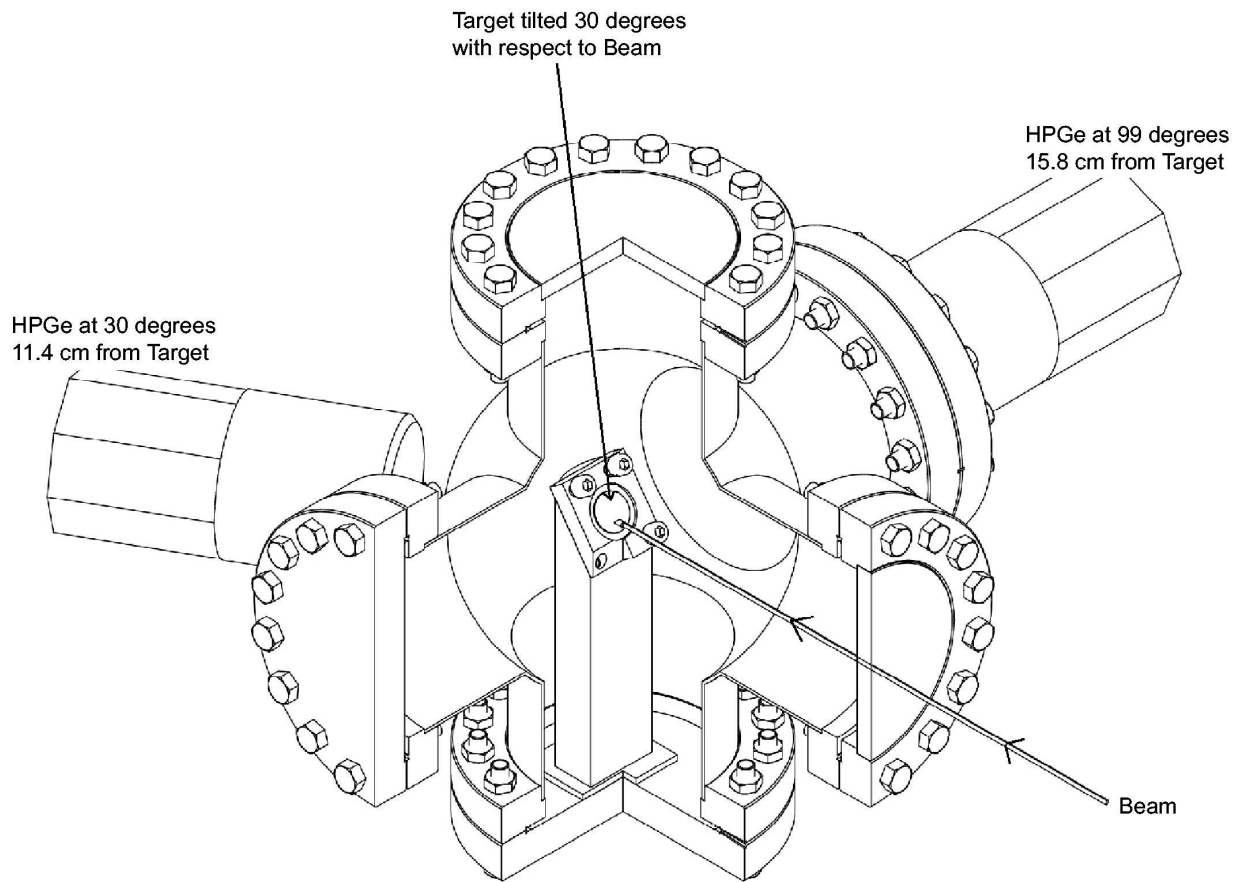Fig. 1.— Partial decay schemes of ^{44}Ti and its daughter ^{44}Sc.

Target tilted 30 degrees
with respect to Beam

HPGe at 99 degrees
15.8 cm from Target

HPGe at 30 degrees
11.4 cm from Target

Beam

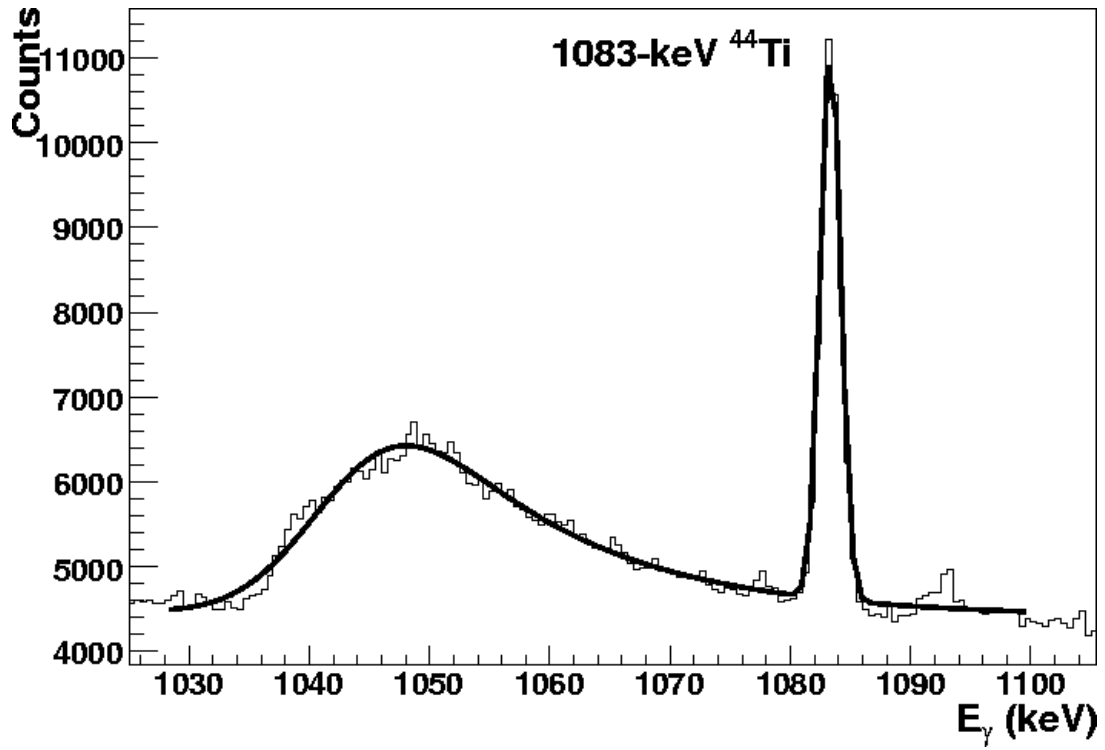Fig. 2.— A Schematic of the target chamber used in the experiment.

Fig. 3.— Partial HPGe γ-ray spectra at $E_\alpha = 5.36$ for the detector at 99° with a simultaneous fit to the 1039 keV ^{70}Ge and 1083 keV ^{44}Ti γ-rays.
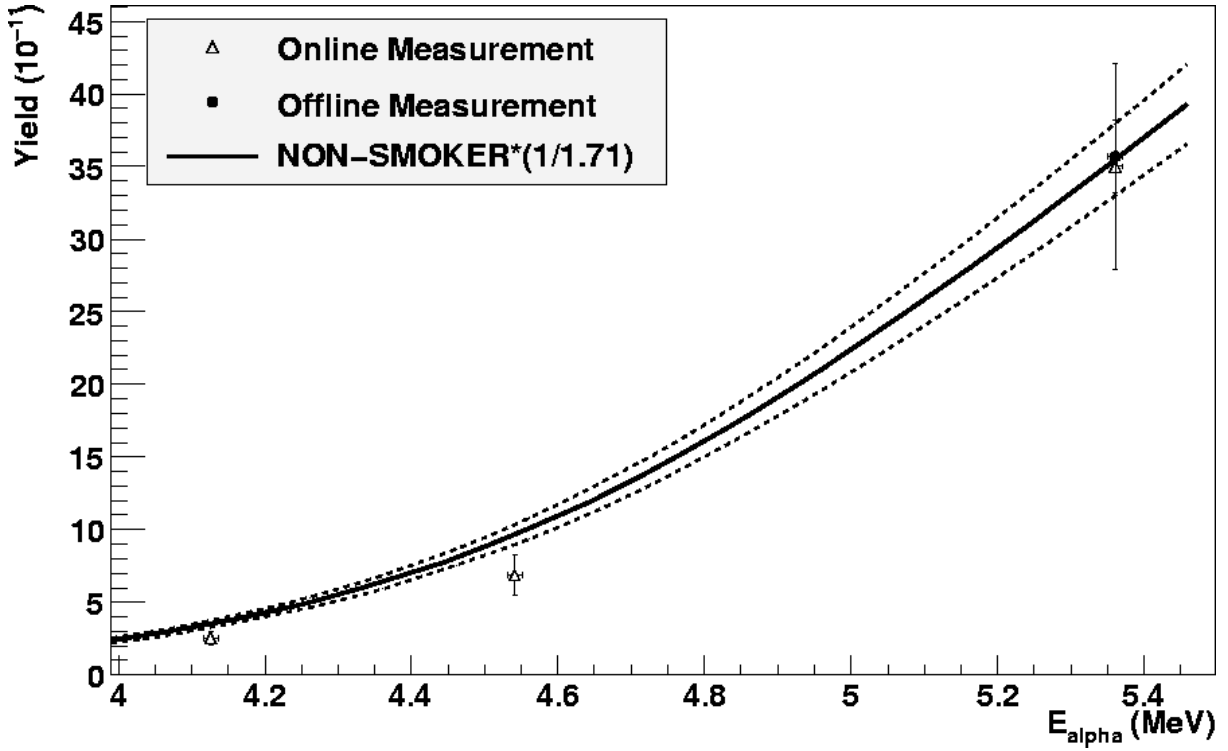
Fig. 4.— Measured thick target yields compared to the calculated NON-SMOKER thick target yield. The online measurement is the measured yield for the 1083 keV γ-ray corrected upward by 20% (see the text). The $E_\alpha = 5.36$ MeV offline counting data point and its error is plotted as measured. The NON-SMOKER cross section required a downward scaling of 1.71 to match the off-line data point. The dashed lines indicate the normalization needed to match the offline error bars.
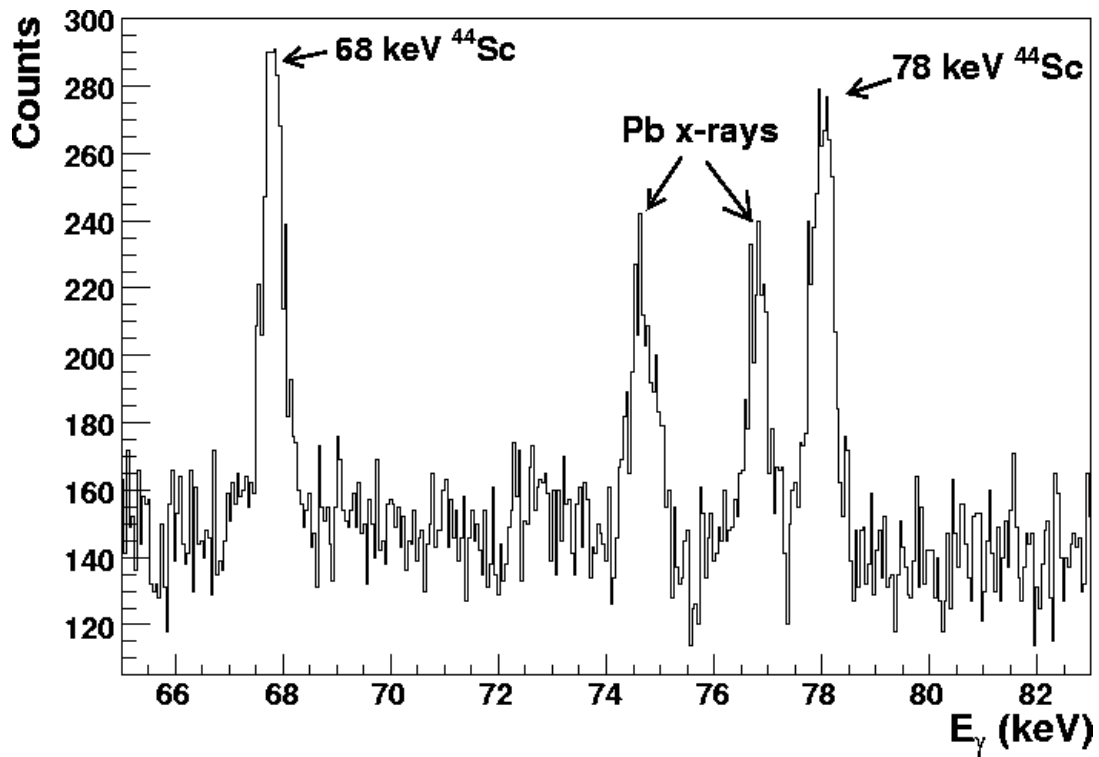
Fig. 5.— γ-ray spectra observed in a two week low background count of the activated target bombarded at $E_\alpha = 5.36$ MeV.
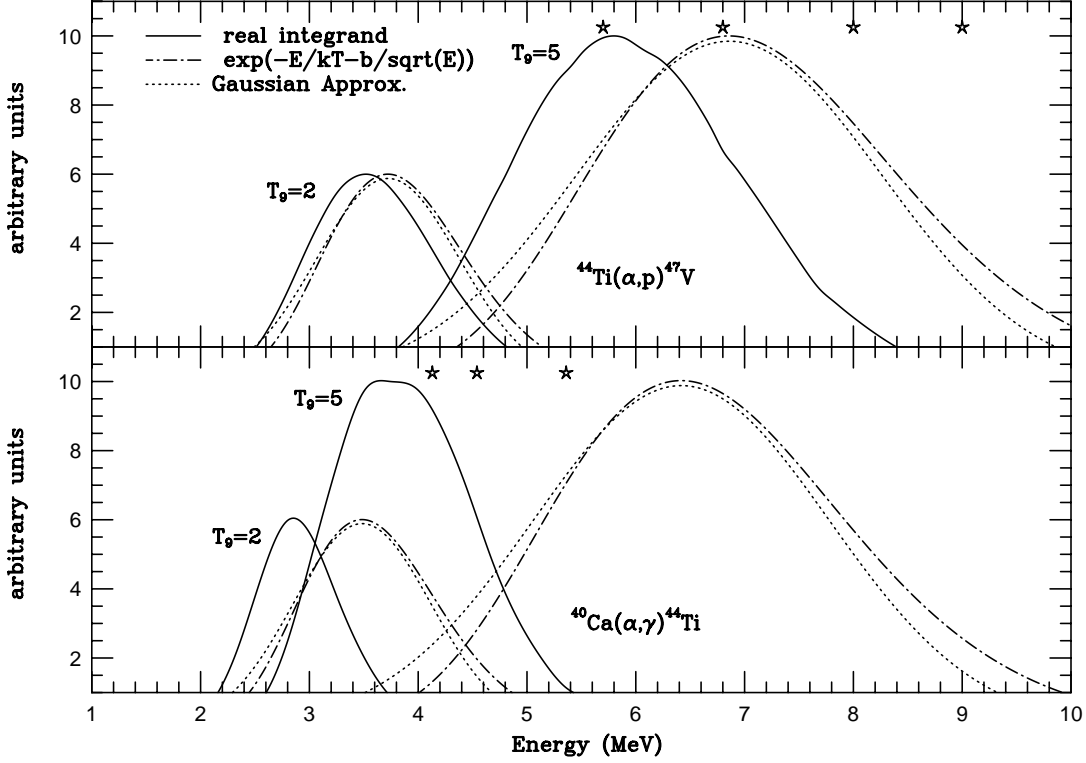
Fig. 6.— The Effective Gamow windows for ^{40}Ca$(\alpha,\gamma)^{44}$Ti and ^{44}Ti$(\alpha,p)^{47}$V at $T_9 = 2$ and $T_9 = 5$. Shown are the true Gamow window as given by the real integrand of the reaction rate formula (solid line type, see Eq. 4), the product of the high-energy tail of the Maxwell-Boltzmann distribution with the simple Coulomb barrier penetration factor (denoted as "exp(-E/kT-b/sqrt(E)), dot-dash line type)" and the usual Gaussian approximation to the latter ("Gauss approx", dotted line type). Stars denote the energy values at which experimental data were measured in our effort and from Sonzogni et al. (2000). The Gaussian approximation is widely used to estimate the Gamow window but predicts it at too high an energy, especially for the capture reaction. For purposes of illustration, all curves were renormalized to the arbitrary unit scale shown, for $T_9 = 5$ all three quantities peak at 10, for $T_9 = 2$ they peak at 6.
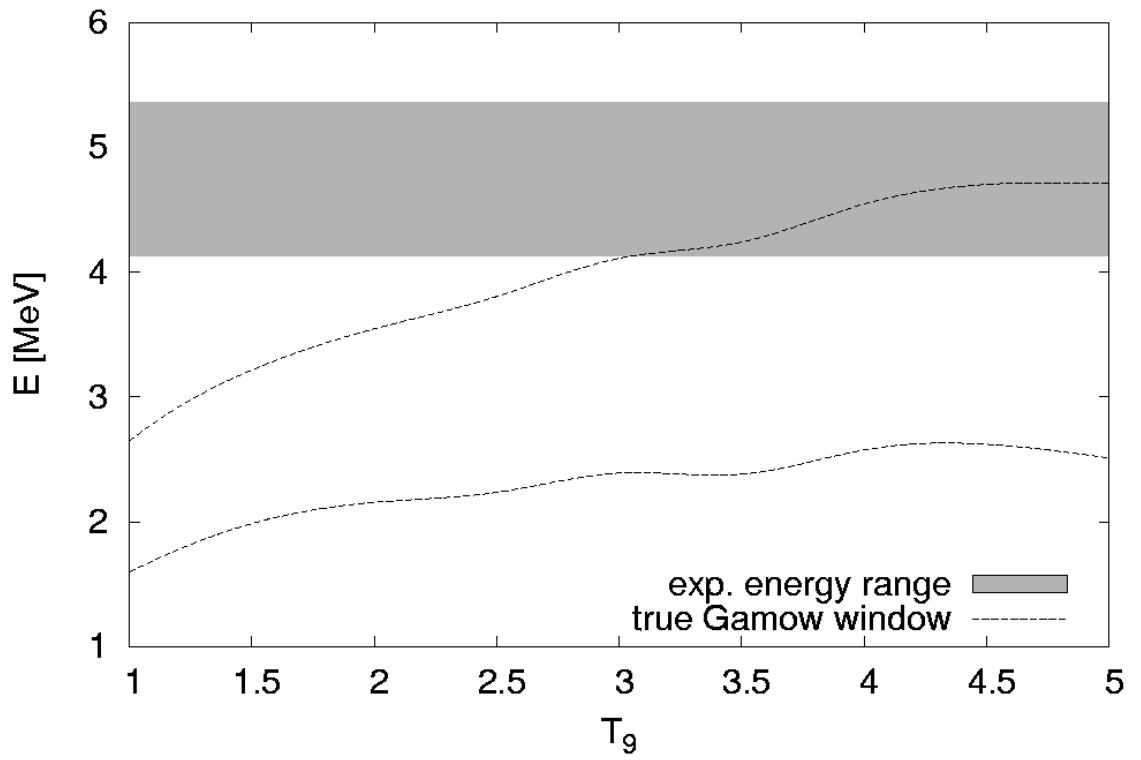
Fig. 7.— Comparison of the experimental energy range for ^{40}Ca(α,γ)^{44}Ti with the true Gamow window given by the actual maximal contributions to the reaction rate integral. The experimental data do not contribute significantly to the rate in the temperature range relevant to ^{44}Ti synthesis ($2.0 \leq T_9 \leq 4.0$).
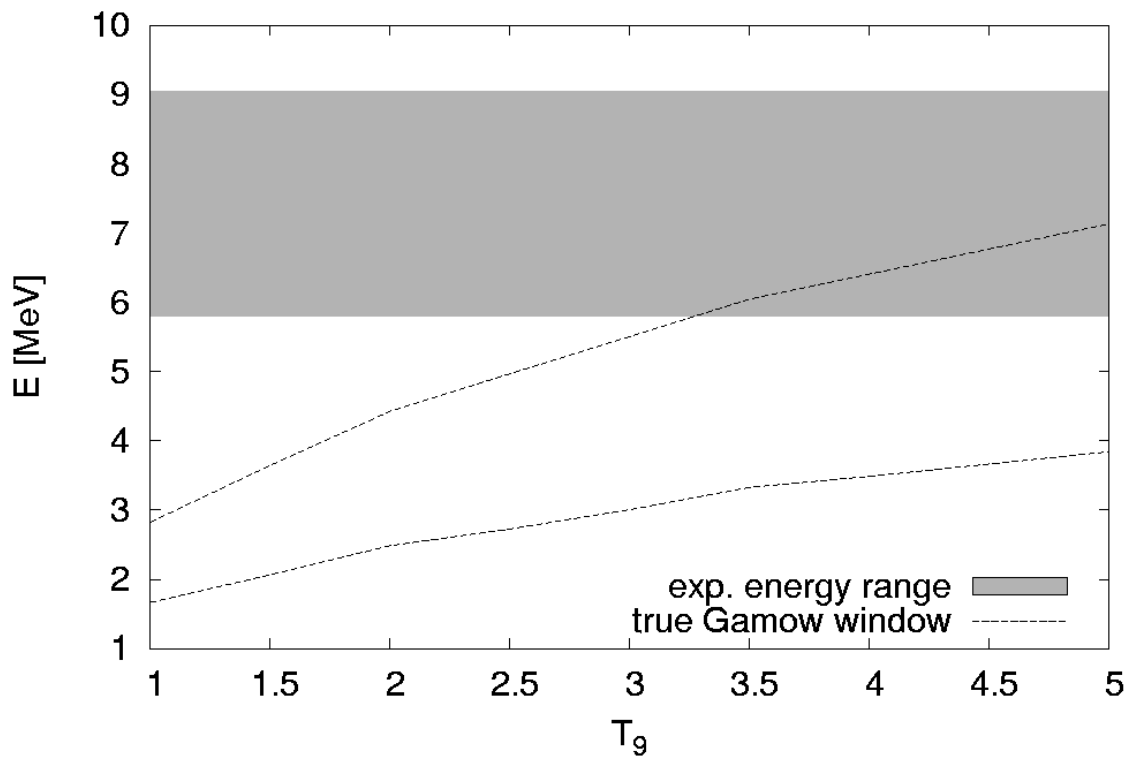
Fig. 8.— Same as Figure 7 but for the ^{44}Ti(α,p)^{47}V reaction.
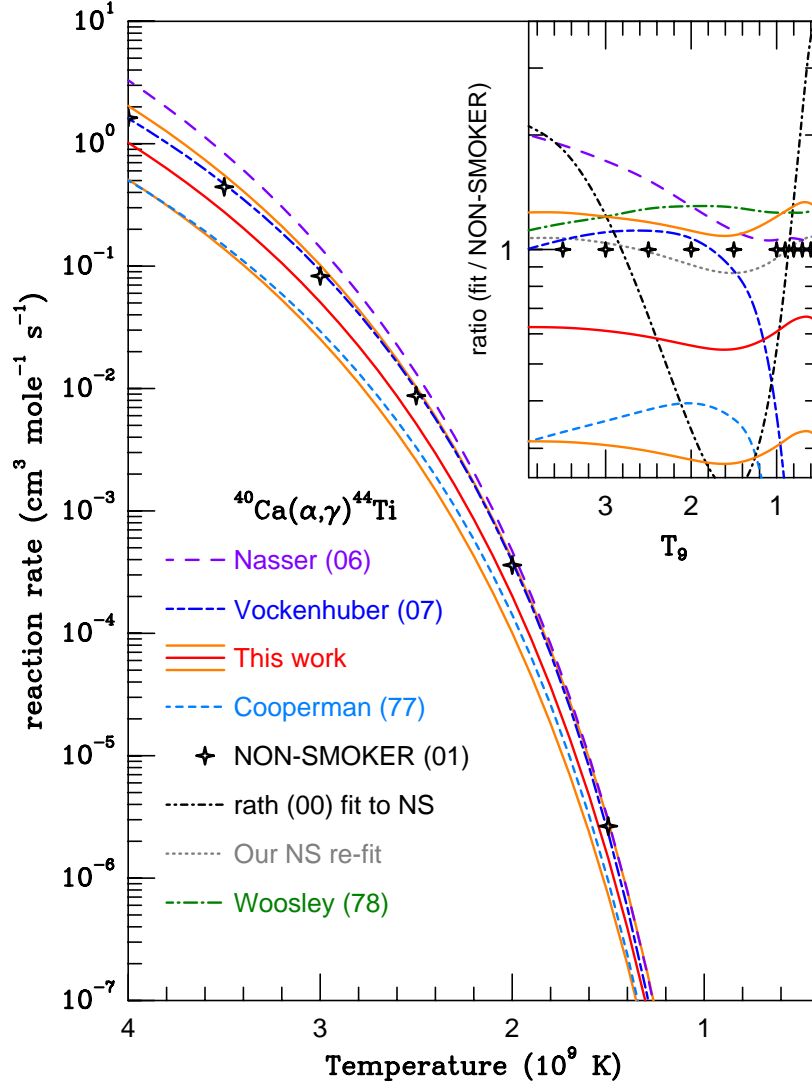
Fig. 9.— Fits to reaction rates for ^{40}Ca$(\alpha,\gamma)^{44}$Ti considered in this study. Solid and dashed line types denote experimental rates from various authors, dotted and dot-dash line types are from various theory efforts. The tabulated NON-SMOKER theory rate (Rauscher & Thielemann 2001) is denoted by crosses. Our recommended rate (and its error, $\pm \times 2$) are indicated as solid (lighter) lines. The inset illustrates the ratio of each reaction rate to the NON-SMOKER rate, including the (dot-short-dash) original fit (Rauscher & Thielemann 2000), our attempt (dotted) to refit the tabulated NON-SMOKER rate, and the theory rate (dot-long-dash) of Woosley et al. (1978).
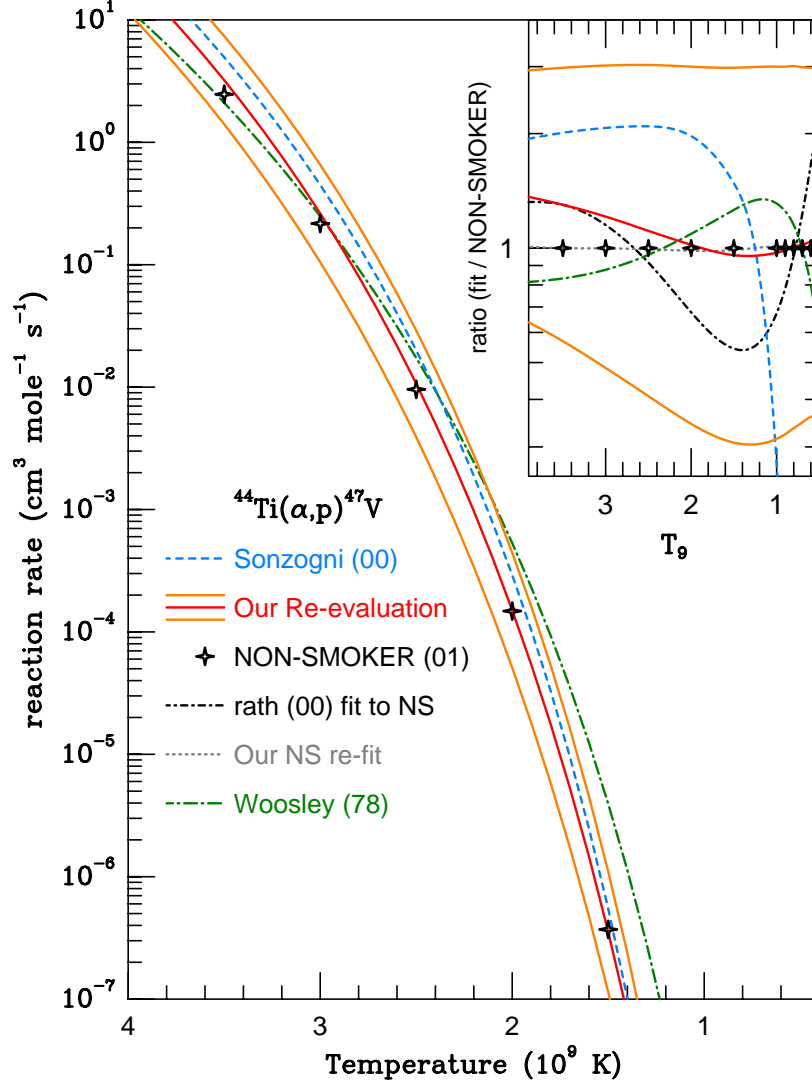
Fig. 10.— Fits to reaction rates for ^{44}Ti$(\alpha,p)^{47}$V considered in this study. Solid line type denotes our re-evaluation and its likely error ($\pm \times 3$) of the lone experimental rate (dashed-line type) of Sonzogni et al. (2000), while the tabulated NON-SMOKER theory rate (Rauscher & Thielemann 2001) is denoted by crosses. The inset illustrates the ratio of each reaction rate to the NON-SMOKER rate, including the (dot-short-dash) original fit (Rauscher & Thielemann 2000), our attempt (dotted) to refit the tabulated NON-SMOKER rate, and the theory rate (dot-long-dash) from Woosley et al. (1978).
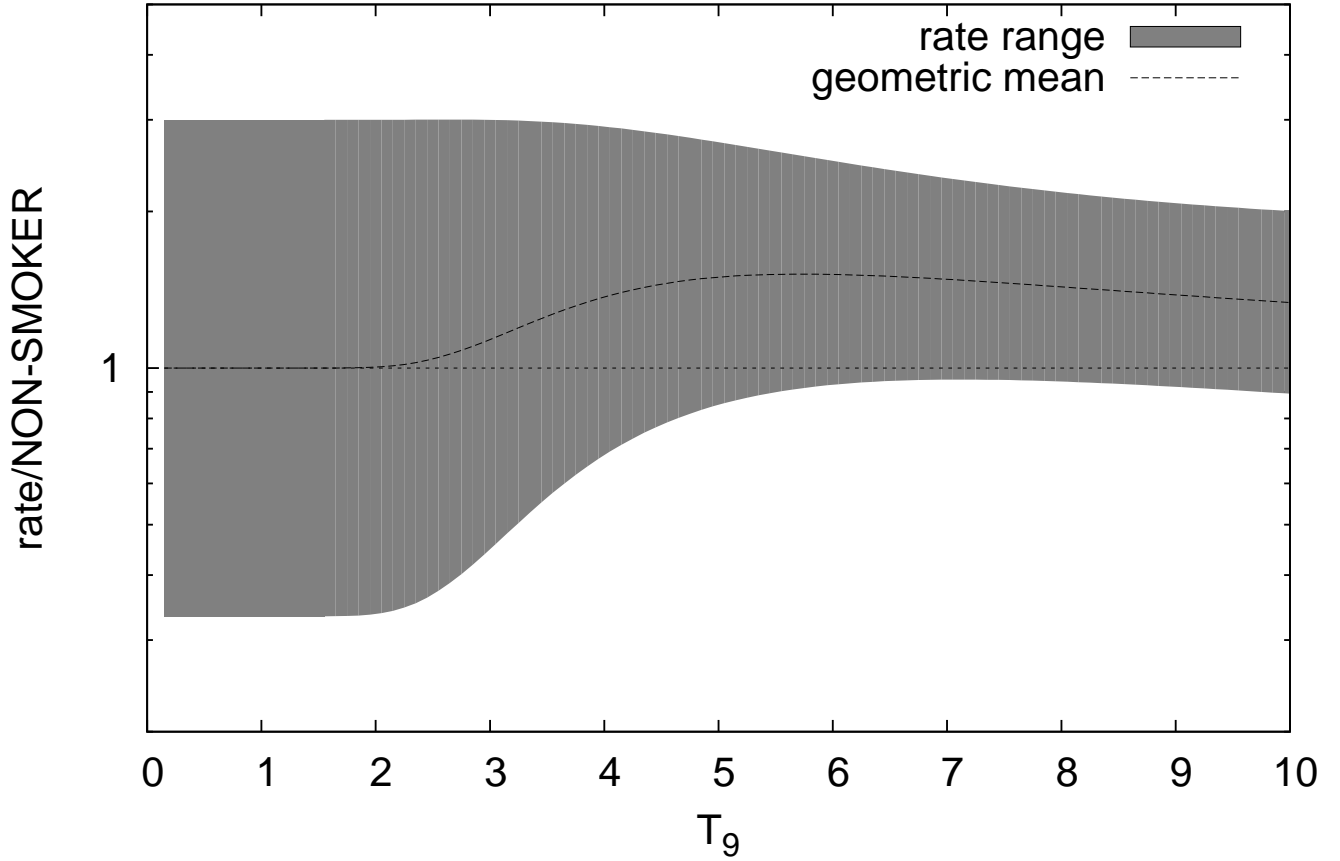
Fig. 11.— Re-evaluated ^{44}Ti$(\alpha,p)^{47}$V rate, based on data by Sonzogni et al. (2000): Ratio of the new rate to the NON-SMOKER rate (Rauscher & Thielemann 2001). The estimated range of the rate is derived from the theoretical and experimental errors (see the text for details). The geometric mean of the upper and lower limit is used as a recommended rate in this work. The impact of the Sonzogni et al. (2000) data manifests itself in the deviation of the geometric mean from unity. Within errors, the new rate is compatible with the NON-SMOKER rate.
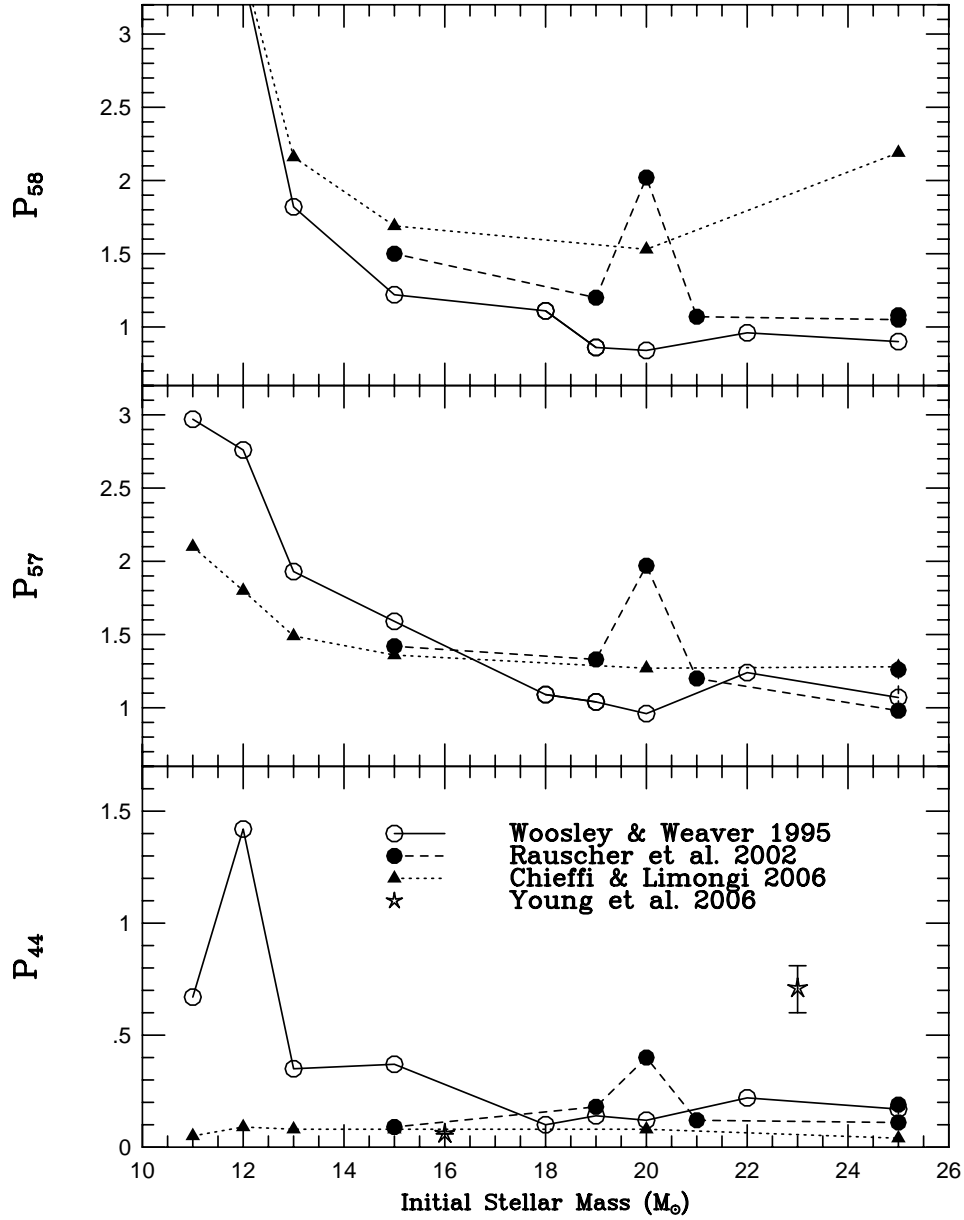
Fig. 12.— Normalized production factors for ^{44}Ti, ^{57}Ni and ^{58}Ni versus initial stellar mass derived from nucleosynthetic yields of SN models (Woosley et al. 1995; Rauscher et al. 2002; Limongi & Chieffi 2006; Young et al. 2006).
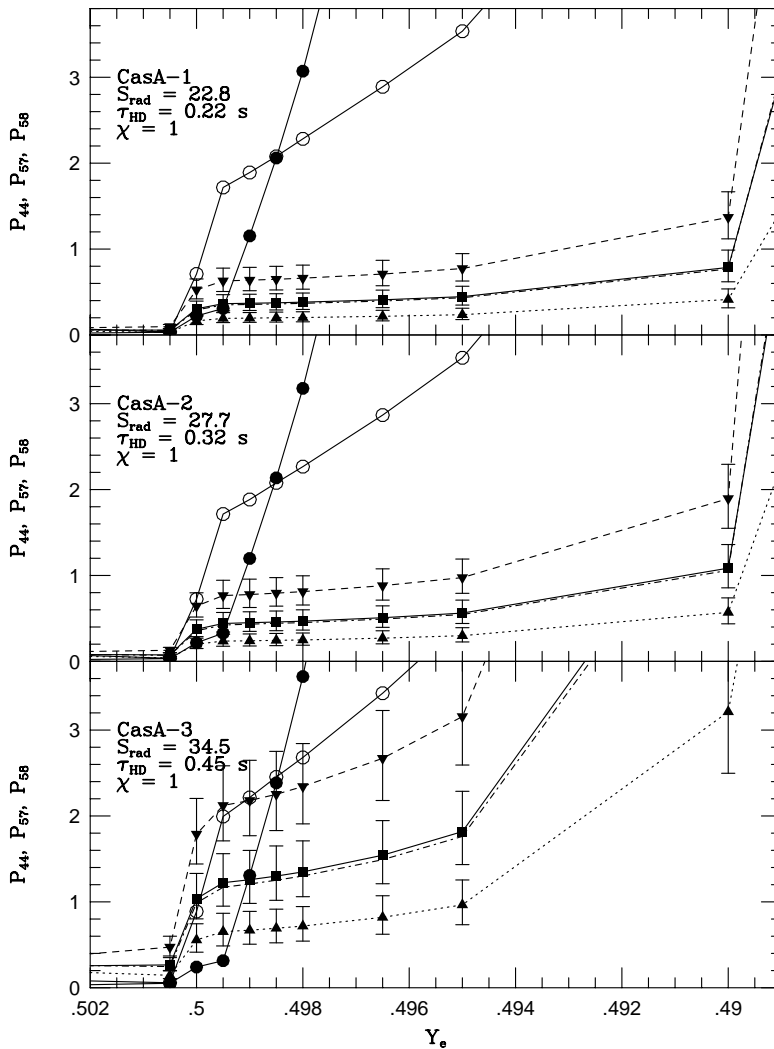
Fig. 13.— Normalized production factors for ^{44}Ti, ^{57}Ni, and ^{58}Ni versus Y_e for adiabatic freeze outs from peak conditions CasA $1-3$ in Table 5. All points were drawn from a model for Cassiopia A (Magkotsios et al. 2008). Each central point represents a calculation that utilizes our recommended "semi-experimental" reaction rate for ^{40}Ca$(\alpha, \gamma)^{44}$Ti and three choices of ^{44}Ti$(\alpha, p)^{47}$V reaction rate from our re-evaluation of the experimental effort of Sonzogni et al. (2000): our "recommended" ^{44}Ti$(\alpha, p)^{47}$V rate (solid line, filled squares), and its upper and lower bound (denoted by filled triangles with dotted and dashed line styles, respectively). Error bars on each point reflect the minimum and maximum deviations of P_{44} due to variations of the six other ^{40}Ca$(\alpha, \gamma)^{44}$Ti reaction rates we considered. The dot-short-dash line shows ^{44}Ti synthesis using the original fits of Rauscher & Thielemann (2000) for both ^{40}Ca$(\alpha, \gamma)^{44}$Ti and ^{44}Ti$(\alpha, p)^{47}$V. For the two NPF's P_{57} and P_{58} (shown as open and filled circles, respectively) an upper bound of 3 limits the allowed range of Y_e.
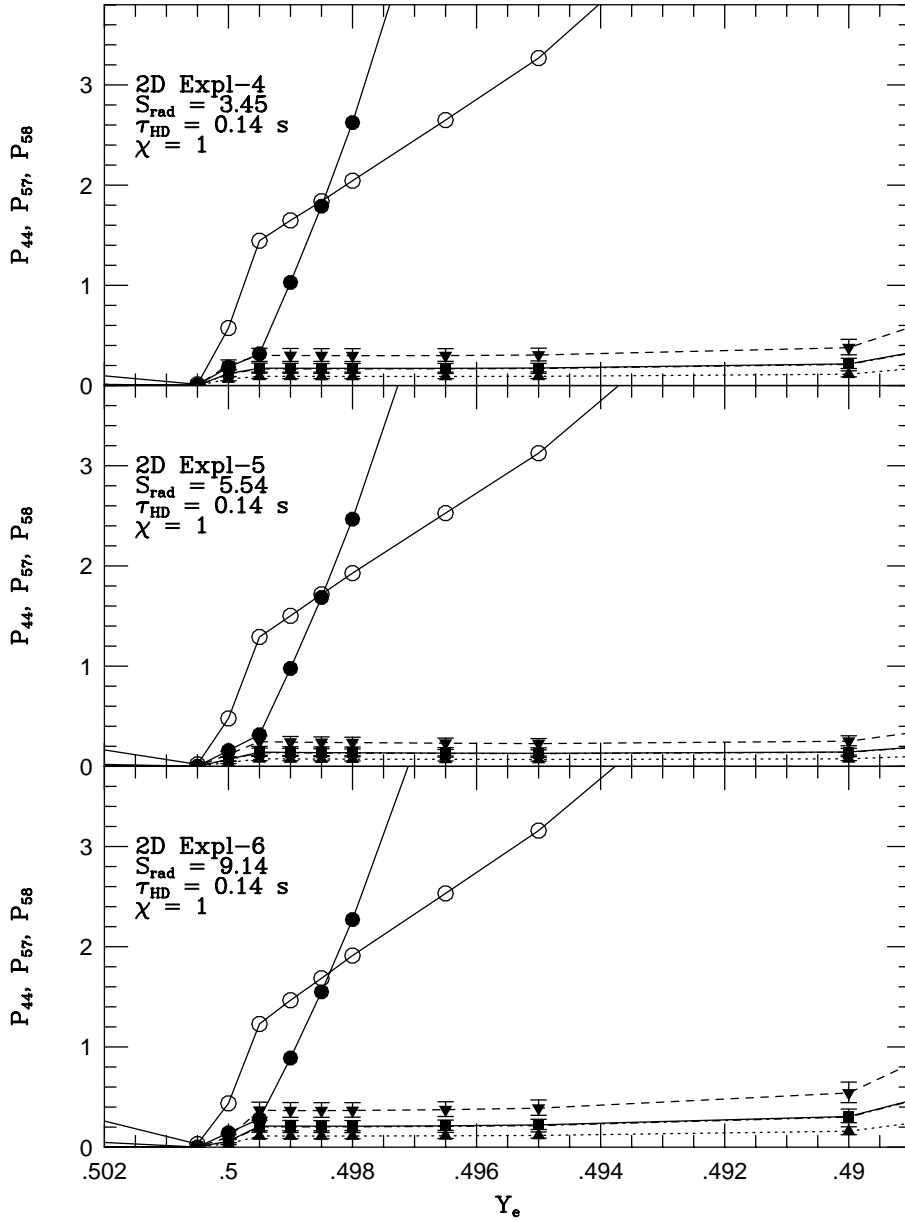
Fig. 14.— Same as Figure 13 but for peak conditions $4 - 6$ in Table 5 drawn from a rotating two-dimensional explosion model (Magkotsios et al. 2008). The production of ^{57,58}Ni with respect to solar iron is nearly the same as in the model for CasA, but the production of ^{44}Ti is substantially lower in every case due to the lower entropy experienced in these expansions.
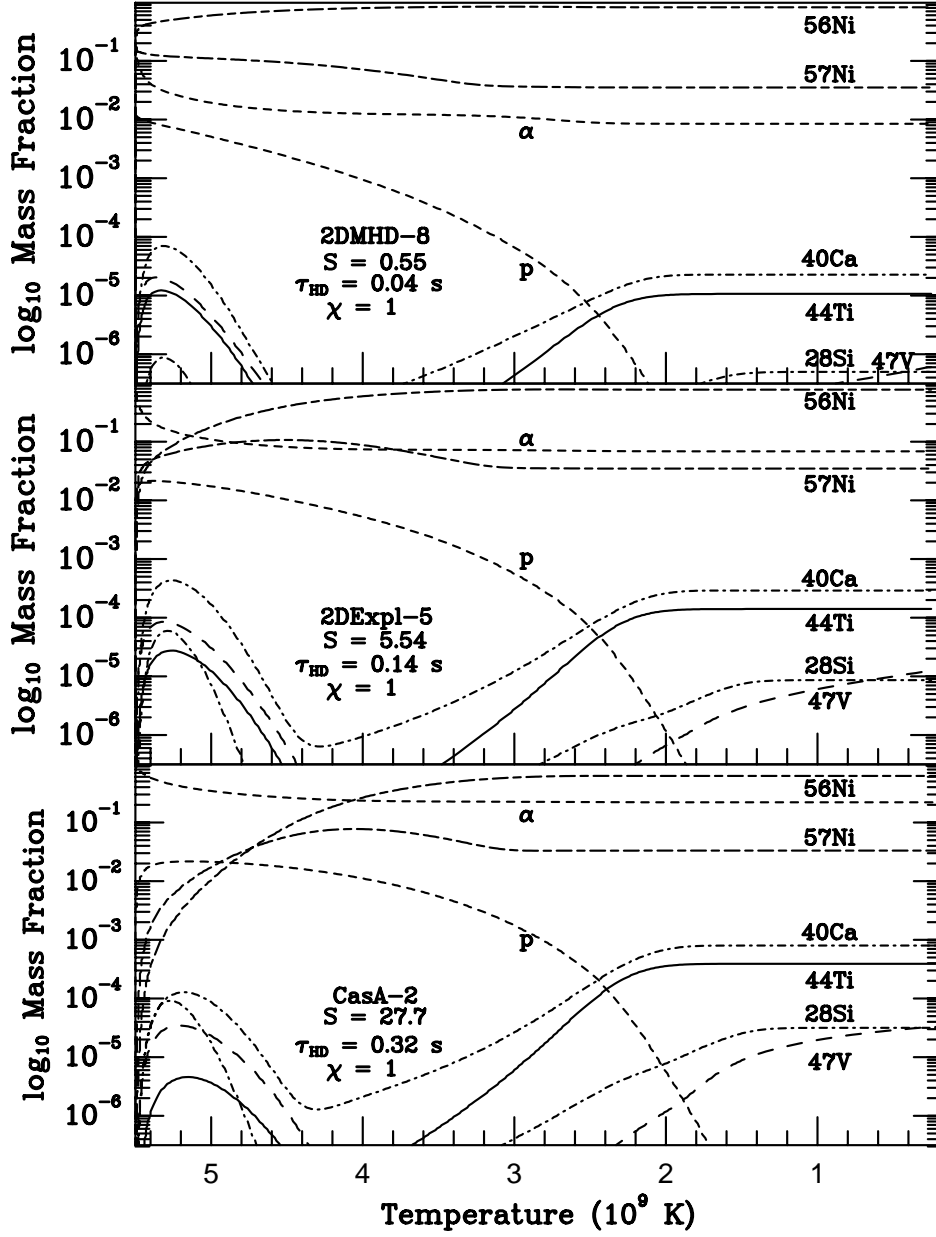
Fig. 15.— Evolution of select mass fractions versus temperature during freeze outs with identical peak temperatures ($T_{9p} = 5.5$) and electron fractions ($Y_e = 0.4980$), but different intial peak densities, for three points in our survey. The higher entropy expansions produce less ^{56}Ni and have a higher α-particle mass fraction at late times that facilitates the re-assembly of species below the iron group, including ^{40}Ca and ^{44}Ti.
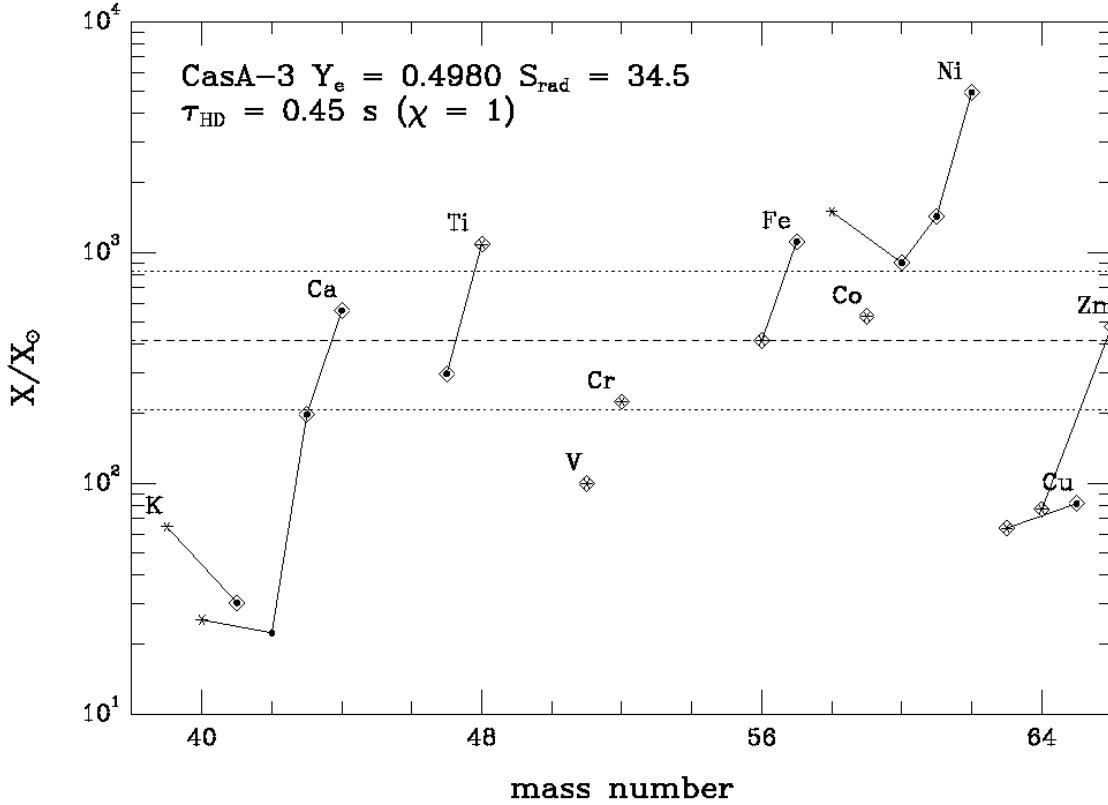
Fig. 16.— Production factors (final decayed mass fractions divided by their abundances in the Sun) repre-senting the range of species produced in the α-rich freeze-out from peak conditions for point CasA-3 in Table 5 assuming our "recommended" reaction rates for $^{40}\mathrm{Ca}(\alpha, \gamma)^{44}\mathrm{Ti}$ and $^{44}\mathrm{Ti}(\alpha, p)^{47}\mathrm{V}$. This is for the specific case of $Y_e = 0.4980$ and $\chi = 1$. This is a fairly typical nucleosynthesis pattern over the range of allowed Y_e for the α-rich freeze outs in the CasA and two-dimensional explosion models we consider.
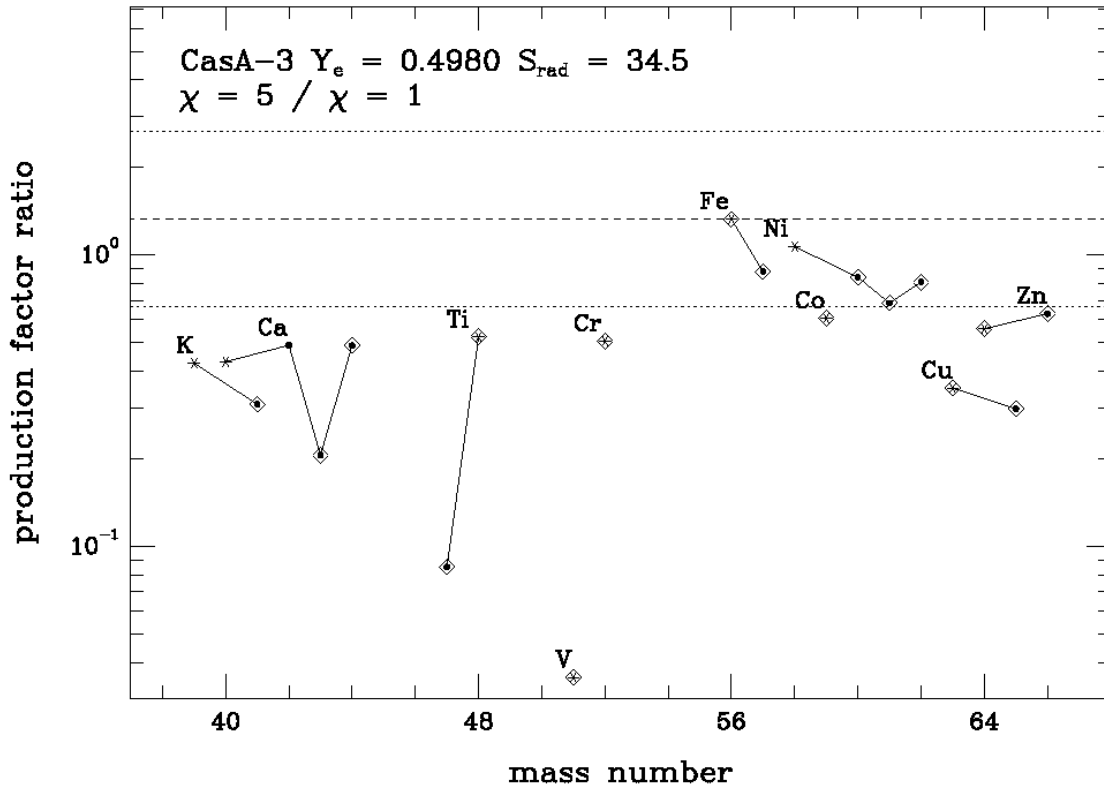
Fig. 17.— Similar to Figure 16, this is the ratio of the production factors for two scalings on the hydrodynamic time-scale, default ($\chi = 1$) and extended ($\chi = 5$). The species created in NSE are much less affected than the lighter isotopes which are reassembled for $2 \leq T_9 \leq 4$.
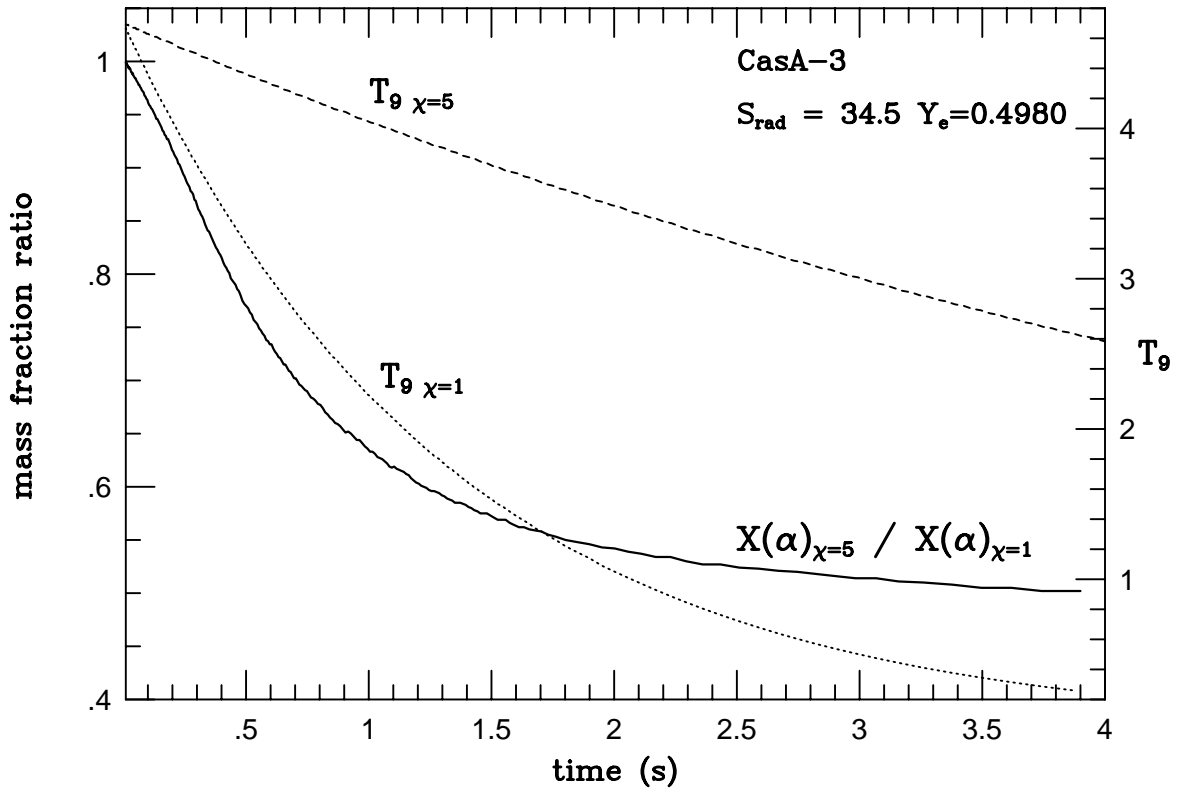
Fig. 18.— Temperature evolution in the CasA-3 expansion assuming two scalings on the hydrodynamic time-scale, default ($\chi = 1$) and extended ($\chi = 5$). Also shown is the ratio of the α-particle mass fraction.
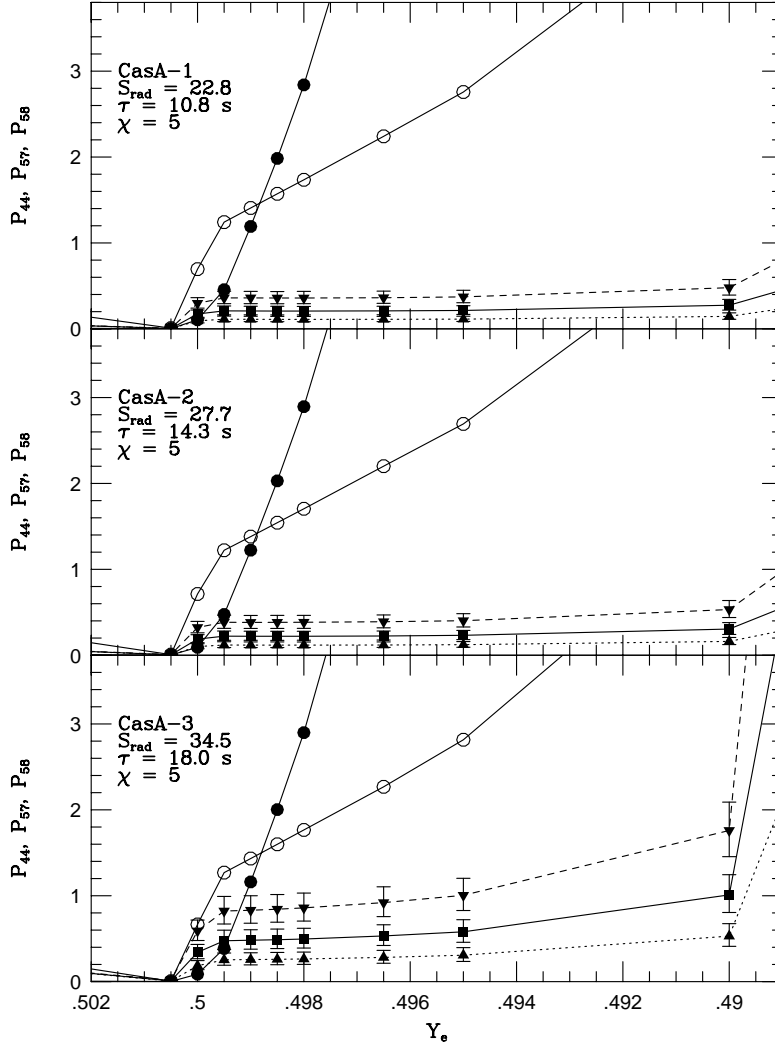
Fig. 19.— Normalized production factors for ^{44}Ti, ^{57}Ni, and ^{58}Ni versus Y_e for adiabatic freeze outs from peak conditions CasA $1-3$ in Table 5 but with an assumed $\chi = 5$ scaling of the hydrodynamic timescale. Results for the Ni isotopes are very similar to the default ($\chi = 1$) scaling case (Figure 13), but due to the longer time spent at high temperature, the α-particle abundance at the onset of ^{40}Ca assembly was much lower ($\sim 40\%$) than in the default scaling case, which facilitated a much lower final value for P_{44} in all cases studied.